

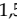
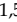



Research Paper

Highly potent and selective PPAR δ agonist reverses memory deficits in mouse models of Alzheimer's disease

Hyeon Jeong Kim¹, Haelee Kim², Jaeyoung Song², Jun Young Hong^{3,4}, Elijah Hwejin Lee^{1,5}, Ashwini M. Londhe^{1,5}, Ji Won Choi¹, Sun Jun Park⁶, Eunseok Oh³, Heeseok Yoon², Hoosang Hwang³, Dongyup Hahn^{3,7}, Kyungjin Jung², Sugyeong Kwon², Tara Man Kadayat², Min Jung Ma², Jeongmin Joo², Jina Kim², Jae Hyun Bae², Hayoung Hwang², Ae Nim Pae^{1,5}, Sung Jin Cho⁶, Jong-Hyun Park^{1,5}, Jungwook Chin^{2,6}, Heonjoong Kang^{3,8}, Ki Duk Park^{1,5}

1. Center for Brain Disorders, Korea Institute of Science and Technology (KIST), Seoul 02792, Republic of Korea.
2. New Drug Development Center, Daegu-Gyeongbuk Medical Innovation Foundation, Daegu 41061, Republic of Korea.
3. Laboratory of Marine Drugs, School of Earth and Environmental Sciences, Seoul National University, NS-80 Seoul 08826, Republic of Korea.
4. Department of Systems Biology, Yonsei University, Seoul 03722, Republic of Korea.
5. Division of Bio-Medical Science & Technology, KIST School, Korea University of Science and Technology, Seoul 02792, Republic of Korea.
6. Cureverse, Inc., H2 building, KIST, Seoul 02792, Republic of Korea.
7. School of Food Science and Biotechnology, Kyungpook National University, Daegu 41566, Republic of Korea.
8. Research Institute of Oceanography, Seoul National University, NS-80, Seoul 08826, Republic of Korea.

 Corresponding authors: Ki Duk Park, Ph.D., Center for Brain Disorders, Korea Institute of Science and Technology (KIST), Seoul 02792, Republic of Korea. ORCID iD: <https://orcid.org/0000-0002-7753-214X>; Tel.: +82-2-958-5132; Fax: +82-2-958-5189; E-mail: kdpark@kist.re.kr. Heonjoong Kang, Ph.D., Laboratory of Marine Drugs, School of Earth and Environmental Sciences, Seoul National University, NS-80 Seoul 08826, Republic of Korea. Tel.: +82-2-880-5730; Fax: +82-2-883-9289; E-mail: hjkang@snu.ac.kr. Jungwook Chin, Ph.D., New Drug Development Center, Daegu-Gyeongbuk Medical Innovation Foundation, Daegu 41061, Republic of Korea, Cureverse, Inc., H2 building, KIST, Seoul 02792, Republic of Korea. ORCID iD: <https://orcid.org/0000-0001-6060-0508>; Tel.: +82-53-790-5257; Fax: +82-2-958-5189; E-mail: jwchin@kist.re.kr. Jong-Hyun Park, Ph.D., Center for Brain Disorders, Korea Institute of Science and Technology (KIST), Seoul 02792, Republic of Korea. ORCID iD: <https://orcid.org/0000-0001-9711-0270>; Tel.: +82-2-958-6979; Fax: +82-2-958-5189; E-mail: jhyunprk@kist.re.kr.

© The author(s). This is an open access article distributed under the terms of the Creative Commons Attribution License (<https://creativecommons.org/licenses/by/4.0/>). See <http://ivyspring.com/terms> for full terms and conditions.

Received: 2024.03.28; Accepted: 2024.09.06; Published: 2024.09.16

Abstract

Rationale: Alzheimer's disease (AD) is a progressive neurodegenerative disease accompanied by neurotoxicity, excessive inflammation, and cognitive impairment. The peroxisome proliferator-activated receptor (PPAR) δ is a potential target for AD. However, its regulatory mechanisms and therapeutic potential in AD remain unclear. We aimed to investigate if the activation of PPAR δ using a highly selective and potent agonist could provide an effective therapeutic strategy against AD.

Methods: We synthesized a novel PPAR δ agonist, **5a**, containing a selenazole group and determined the X-ray crystal structure of its complex with PPAR δ . The drug-like properties of **5a** were assessed by analyzing cytochrome P450 (CYP) inhibition, microsomal stability, pharmacokinetics, and mutagenicity. We investigated the anti-inflammatory effects of **5a** using lipopolysaccharide (LPS)-stimulated BV-2 microglia and neuroinflammatory mouse model. The therapeutic efficacy of **5a** was evaluated in AD mice with scopolamine-induced memory impairment and APP/PS1 by analyzing cognitive function, glial reactivity, and amyloid pathology.

Results: Compound **5a**, the most potent and selective PPAR δ agonist, was confirmed to bind hPPAR δ in a complex by X-ray crystallographic analysis. PPAR δ activation using **5a** showed potent anti-inflammatory effects in activated glial cells and mouse model of neuroinflammation. Administration of **5a** inhibited amyloid plaque deposition by suppressing the expression of neuronal beta-site amyloid precursor protein cleaving enzyme 1 (BACE1), and reduced abnormal glial hyperactivation and inflammatory responses, resulting in improved learning and memory in the APP/PS1 mouse model of AD.

Conclusion: We identified that specific activation of PPAR δ provides therapeutic effects on multiple pathogenic phenotypes of AD, including neuroinflammation and amyloid deposition. Our findings suggest the potential of PPAR δ as a promising drug target for treating AD.

Keywords: PPAR δ agonist, Alzheimer's disease, anti-inflammation, glial activation, BACE1

Introduction

Peroxisome proliferator-activated receptors (PPARs) are nuclear transcriptional factors belonging to the ligand-activated nuclear receptor superfamily and consist of three known subtypes: PPAR α , γ , and δ [1,2]. Upon activation, these receptors heterodimerize with retinoid X receptor and regulate the expression of genes involved in energy utilization, cell differentiation, proliferation, mitochondrial function, glucose homeostasis, and lipid metabolism [3-5]. Thus, PPARs have been mainly studied in muscle or peripheral organs as therapeutic targets for drugs against cancer, cardiovascular disease, and metabolic disorders such as diabetes [5-7].

PPAR δ , also known as PPAR β , is ubiquitously expressed in murine and human tissues, being more abundant in the brain than other PPAR subtypes [8-10]. PPAR δ is expressed in most brain cell types, including neurons, astrocytes, and microglia [11-13], where it regulates neurogenesis, oxidative stress, neuroinflammation, as well as lipid metabolism [14-18]. In mouse models of neurodegenerative disease or ischemic stroke, PPAR δ agonists suppress neuronal cell loss [19,20], mitochondrial dysfunction [20], activation of nuclear factor (NF)- κ B or nucleotide-binding domain and leucine-rich-repeat-protein 3 (NLRP3) inflammasome [21,22], and neutrophil infiltration [23, 24] and reduce the expression of several pro-inflammatory chemokines and cytokines such as tumor necrosis factor (TNF)- α and interleukin (IL)-6 [21, 24]. These results indicate that PPAR δ agonists exert potent neuroprotective and anti-inflammatory effects in the central nervous system (CNS). PPAR δ -null mice and transgenic mice expressing dominant-negative PPAR δ in neurons exhibit fatal defects such as brain atrophy, myelin alternation, impaired brain development, and widespread neurodegeneration [19, 25, 26]. Despite its obvious pivotal role in the CNS, the underlying protective mechanism of PPAR δ against neurodegeneration and neuroinflammation remains elusive.

Alzheimer's disease (AD) is the most frequent neurodegenerative disease and is characterized by pathological features such as the deposition of amyloid β (A β) plaques and neurofibrillary tangles and clinical symptoms such as progressive memory loss and cognitive decline [27]. Excessive neuroinflammation, accompanied by hyperactivation of glial cells and prolonged release of inflammatory mediators, is considered an early key event exacerbating the pathogenesis and progression of AD [28, 29]. The level of PPAR δ expression is significantly lower in the brains of patients with AD than in those

of the general population. Similar results are observed in mice with AD compared to their non-AD counterparts [30, 31]. Genetic deletion of PPAR δ leads to cognitive impairment with increased levels of enzymes involved in A β deposition, tau hyperphosphorylation, neuroinflammation, and astrogliosis [32]. In mouse models of AD, PPAR δ activation using specific agonists reverses the pathological manifestations of AD through anti-inflammatory effects [31, 33-37]. Although no FDA-approved drugs specifically target PPAR δ , a recent exploratory phase IIa clinical trial has reported that the dual PPAR δ / γ agonist T3D-959 improves cognitive function in patients with mild-to-moderate AD [35, 38]. However, long-term use of PPAR γ -activating drugs was associated with side effects [39, 40]. Therefore, highly selective PPAR δ agonists are desirable as potential therapeutic agents in AD.

A representative potent and selective PPAR δ agonist that has been developed is GW501516. GlaxoSmithKline discovered and evaluated GW501516 as a drug candidate for treating metabolic and cardiovascular diseases [6]. However, owing to concerns about side effects related to its PPAR γ -activating efficacy, the clinical trial was discontinued [40, 41]. Based on these data, we first synthesized various derivatives of GW501516 to develop a highly potent and selective PPAR δ agonist. Among them, the PPAR δ agonist **5a** containing selenazole core showed excellent agonistic effect and selectivity for PPAR δ . We studied the structure of the complex **5a**-hPPAR δ using X-ray crystallographic analysis and further investigated the therapeutic effects of **5a** on neuroinflammation and AD-like pathology using cellular and mouse models.

Results

Synthesis of novel PPAR δ agonists with a selenazole core

To develop a highly potent and selective PPAR δ agonist, we synthesized various derivatives of GW501516 by introducing a selenium-containing heterocyclic core (Figure 1A). We first optimized the synthesis method for incorporating selenium-containing heterocycles (selenazoles). During this process, we identified that selenocarboxamides played a crucial role in the formation of key intermediates. Specifically, we observed that nitriles react with sodium hydrogen selenide, pyridine, and hydrochloric acid in ethanol, forming primary aryl and alkyl selenocarboxamides [42]. The aryl selenocarboxamide is converted into selenazole following its reaction with methyl-2-chloro-

acetoacetate. We first attempted to prepare the intermediate sulfide/selenide (**3a**, **3b**) from 4-bromo- or 4-iodo-2-methyl phenol **2** as a starting material using the one-pot method that included a four-step reaction: protection of the phenol moiety, lithium-halogen exchange, sulfur/selenium insertion, and quenching of the reaction by adding selenazole (Figure 1B-C).

Starting materials (**2a-c**) were commercially available or easily prepared from *o*-cresol using general halogenation methods. We found that *in-situ* conversion of the phenol group of starting material **2** using *i*PrMgCl (transforming -OH to -O MgCl) offered protection during the lithium-halogen exchange and sulfur/selenium insertion steps. We chose the one-pot method instead of a step-by-step method, which led to a good yield of the intermediate **3**. In the second step, treatment of intermediate **3** with

K₂CO₃ and ethyl bromoacetate in aqueous acetone at room temperature (20–25 °C) for 4 h resulted in ester **4** with high yield (~95%) (Figure 1C). For the final step, hydrolysis of the ethyl ester **4** with 2M LiOH led to compounds **5a** and **5b**, with yields of 92 and 90%, respectively.

The half maximal effective concentration (EC₅₀) values for compounds **5a** and **5b** were derived from an *in vitro* co-transfection assay assessing their affinity and activity towards human PPAR subtypes (Table 1). Our synthesized PPAR δ agonist **5a** exhibited sub-nanomolar potency (EC₅₀ = 0.7 nM) and excellent selectivity for hPPAR δ (>14,000-fold selectivity over hPPAR α and hPPAR γ), demonstrating similar efficacy and better selectivity compared to GW501516 (EC₅₀ = 1.2 nM and 250-fold selectivity over hPPAR α ; 1,000-fold selectivity over hPPAR γ) (Table 1).

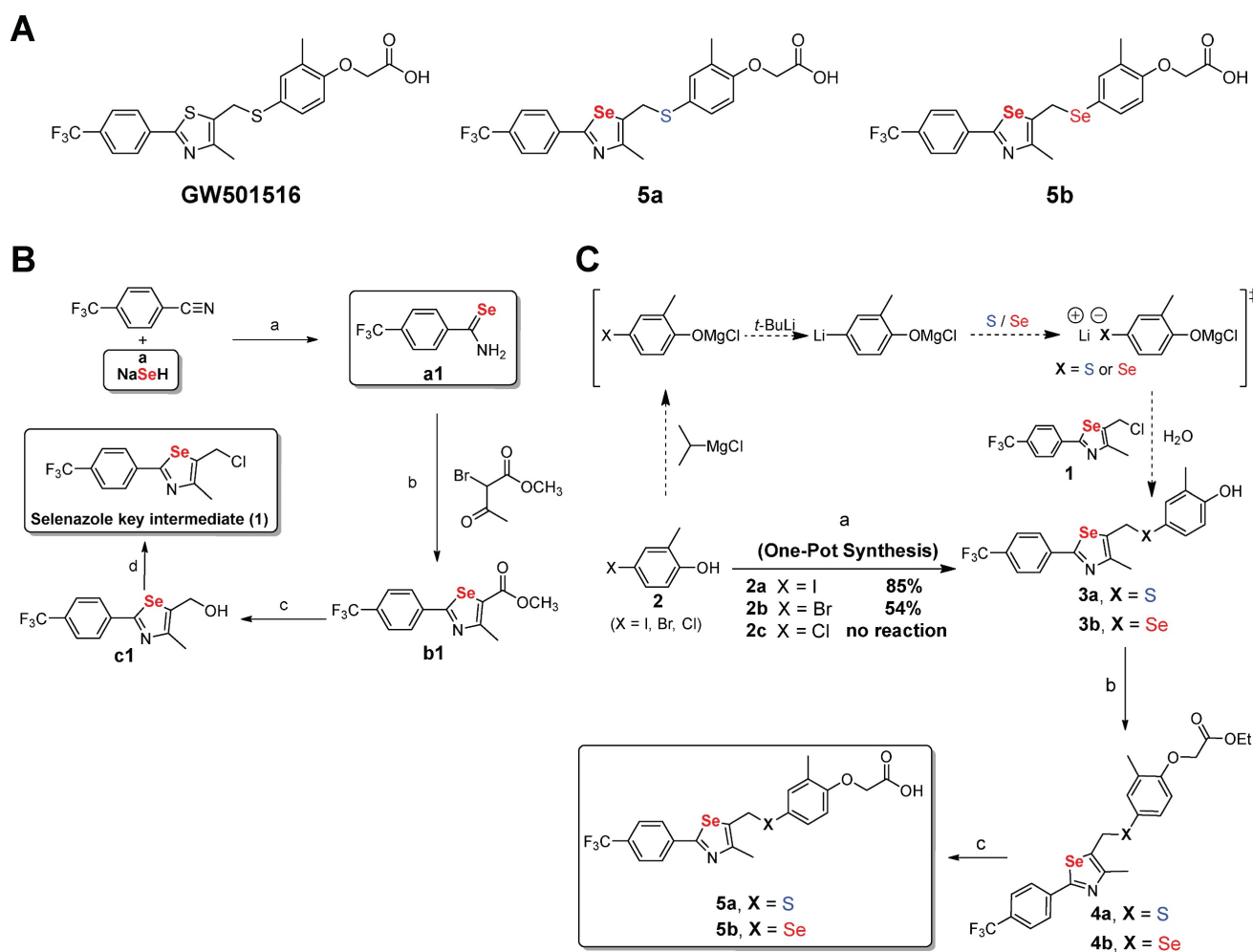


Figure 1. Synthesis of novel PPAR δ agonists containing one selenazole moiety. (A) Structures of GW501516 and PPAR δ agonists with a selenazole core (**5a** and **5b**). (B) Synthesis of key selenazole intermediate. Reagents and conditions: (a) The reaction between HCl 2 M and pyridine/ethanol occurred for 1 h at a temperature varying from room temperature (r.t.) to 100 °C (84%); (b) methyl 2-chloroacetoacetate and tetrahydrofuran (THF) reacted for 12 h at a temperature varying from r.t. to 80 °C (95%); (c) diisobutyl aluminum hydride (DIBAL-H) and dichloromethane (DCM) reacted for 1 h at a temperature varying from -78 to -10 °C (94%); and (d) triphenylphosphine (TPP), DCM, and *N*-chlorosuccinimide (NCS) reacted at r.t. for 10 h (90%). (C) Synthesis of selenium-containing PPAR δ agonists. Reagents and conditions: (a) (i) Isopropylmagnesium chloride (1.0 equiv) and THF reacted at 0 °C for 10 min; (ii) *t*-butyllithium (2.0 equiv) was added at -78 °C for 0.5 h; (iii) sulfur powder (for **3a**) or selenium powder (for **3b**) and THF reacted at -78 to -20 °C for 1 h; (iv) selenazole key intermediate (**1**) and THF reacted at 0 °C for 0.5 h (85%); (b) Ethyl bromoacetate, K₂CO₃ and aq. acetone reacted at r.t. for 4 h (~95%); (c) (i) 2.0 M LiOH and aq. THF reacted at r.t. for 1 h; (ii) the product was acidified with 0.5 M NaHSO₄ (90–92%).

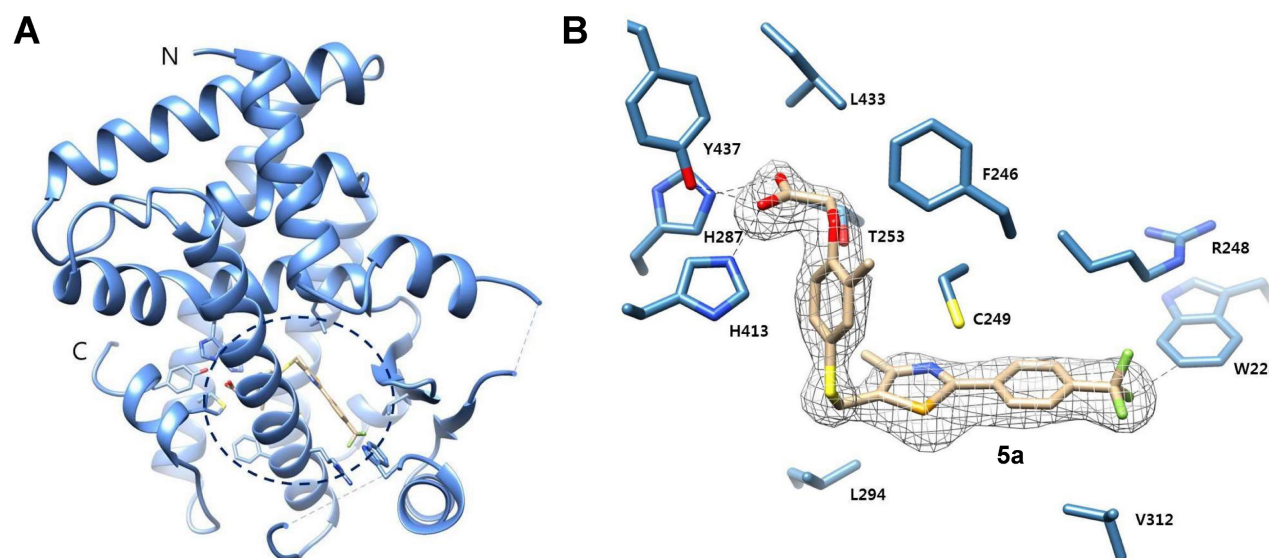


Figure 2. X-ray crystal structure of **5a** bound to the ligand-binding domain (LBD) of human PPAR δ (171 – 441). **(A)** The overall folding of the hPPAR δ -**5a** complex structure. Residues 204–206 and 229–234 are missing due to insufficient electron density. **(B)** Protein residues are represented in blue, while **5a** is designated with beige. An Fo-Fc omit electron density map, contoured at 3.0 σ , is depicted, with the bound ligand shown as a grey mesh. Sulfur is displayed in yellow, selenium in dark yellow, nitrogen in dark blue, oxygen in red, and fluoride in green (PDB code: 5Y7X).

Table 1. Potency and selectivity of GW501516, **5a**, and **5b** for human PPARs.

Compounds	Potency (EC ₅₀ , nM)			Selectivity index*	
	hPPAR α	hPPAR δ	hPPAR γ	hPPAR α /hPPAR δ	hPPAR γ /hPPAR δ
GW501516	300	1.2	1200	250	1000
5a	>10000	0.7	>10000	>14000	>14000
5b	>10000	4.3	>10000	>2300	>2300

*Selectivity index represents the selectivity for the PPAR δ isoform and is given as the ratio of EC₅₀(hPPAR α)/EC₅₀(hPPAR δ) or EC₅₀(hPPAR γ)/EC₅₀(hPPAR δ). EC₅₀: half maximal effective concentration; nd: not determined.

Molecular docking study and X-ray crystallographic analysis of the ligand-human-PPAR δ complexes

Batista *et al.* reported the crystal structure of the PPAR δ -ligand complex, suggesting that VAL312 and ILE328 in the buried hormone-binding pocket play a crucial role in PPAR δ selective binding. Notably, VAL312 and ILE328 in PPAR δ have shorter side chain residues than those in PPAR α (ILE339 and MET355) and PPAR γ (MET348 and MET364) [43].

To explore the binding poses and molecular interactions of compounds **5a** and **5b**, we conducted molecular docking studies. Compounds **5a**, **5b**, and GW501516 exhibited higher binding energy in PPAR δ compared to PPAR α and PPAR γ (Table S1) and showed similar interactions inside the PPAR δ binding site (Figure S1). We subsequently superimposed the binding poses of **5a** inside PPAR δ , PPAR γ , and PPAR α (Figure S2). In the **5a**-PPAR δ complex (magenta), the presence of short residues (VAL312

and ILE238) allows the molecules to fit snugly within the ligand-binding pocket, facilitating a suitable conformation for hydrogen bonding with HIS413, TYR437, and HIS287. Conversely, the long side chains at the corresponding positions in PPAR α and PPAR γ hinder **5a** from adopting a conformation that can form hydrogen bonds with these critical residues (Figure S2).

To clearly understand the binding mode of **5a** in the ligand-binding site, we determined the crystal structure of the ligand-binding domain (LBD) in the complex **5a**-hPPAR δ (171–441) (Figure 2). Compound **5a** binds in the ligand-binding pocket in a similar manner to GW501516 [39]. The acetic acid moiety forms hydrogen bonds with the side chains of H287, H413, and Y437; corresponding bond lengths are 2.8, 2.7, and 2.6 Å, respectively. A pi-sulfur interaction with a bond length of 3.9 Å was observed between the selenazole ring in **5a** and the C249 side chain.

Hydrophobic interactions with side chains of residues L433, T253, F246, L294, V312, and R248 stabilize the complex receptor-**5a**. The trifluoromethyl group in **5a** establishes a weak hydrogen bond (2.9 Å) with the side chain of W228. This interaction was not observed in the co-crystal structure of the complex GW501516-hPPAR δ , which showed a different rotameric conformation of the W228 indole group [39]. The increased potency of **5a** compared to that of GW501516 for hPPAR δ is likely attributable to its additional contacts with the W228 indole ring through a hydrogen bond involving C(sp³)-F-H-C (sp²).

In vitro absorption, distribution, metabolism, excretion, and toxicity (ADMET) and in vivo pharmacokinetic profiles

The drug-like properties of compound **5a** were subsequently measured using a cytochrome P450 (CYP) inhibition test, liver microsomal metabolic stability test, and human Ether-à-go-go related gene (hERG) assay. To identify potential drug-drug interactions, we examined the inhibitory effects of **5a** on five CYP isotypes: 1A2, 2C9, 2C19, 2D6, and 3A4. Compound **5a** exhibited low inhibitory activities against CYP subtypes at 10 μ M ($IC_{50} > 10 \mu$ M) (Table S2). It showed excellent metabolic stability in human liver microsomes and low inhibitory effects on the hERG channel (Table S2). We also investigated the *in vivo* pharmacokinetic (PK) properties of compound **5a** after intravenous injection (*i.v.*) of a dose of 1 mg/kg or oral administration (*p.o.*) of a dose of 10 mg/kg in rats (Table S3). Compound **5a** showed high oral bioavailability ($F = 90.7\%$) with an exceptional AUC value (13331 hr*ng/mL), a substantially high C_{max} value (2744.3 ng/mL), and low plasma clearance ($CL = 10.2$ mL/min/kg).

Next, the mutagenic potential of **5a** was evaluated using a two-strain Ames test, in which *Salmonella typhimurium* strains TA98 and TA100 were used to detect frameshift and base substitution mutations, respectively. Mutagenicity testing indicated that **5a** lacks mutagenicity in the absence as well as in the presence of the S9 fraction in both TA98 and TA100 strains (Table S4). Altogether, these results indicate excellent PK profiles in rats after both *i.v.* and *p.o.* administration and favorable drug-like properties of **5a**.

Compound 5a suppresses inflammatory responses in activated glial cells in vitro

PPAR δ regulates not only lipid metabolism but also inflammatory responses [14-18]. Persistent microglial activation induces neuroinflammation, where excessive release of inflammatory factors causes neuronal cell death, contributing to the progression and severity of AD [28, 29]. To investigate the effect of **5a** on the glial inflammatory responses, we treated BV-2 murine microglial cells with **5a** and GW501516. Compound **5a** did not affect the viability of BV-2 cells up to 20 μ M and was less cytotoxic than GW501516 (Figure 3A). After pretreatment with **5a**, we induced inflammation by treating the cells with LPS and measured the levels of inflammatory mediators. LPS stimulation considerably increased the production of nitric oxide (NO) compared to that in the untreated control; this effect was suppressed by **5a** in a concentration-dependent manner (Figure 3B). Compound **5a** also reduced the LPS-induced

increases in the mRNA and protein levels of inducible nitric oxide synthase (iNOS), a NO-synthesizing enzyme, and pro-inflammatory cytokines such as TNF- α and IL-6 (Figure 3C-E). We also evaluated the effect of **5a** on LPS-induced activation of the NF- κ B p65 subunit that regulates the immune responses and production of inflammatory cytokines. Treatment of LPS increased the phosphorylation of p65, resulting in NF- κ B activation. In contrast, **5a** prevented the increase in level of phosphorylated p65, maintaining its levels at a value similar to that in the LPS-untreated control (Figure 3F).

Besides direct inhibition of NF- κ B, PPAR δ indirectly inhibits the inflammatory responses by inducing the expression of antioxidant enzymes such as heme oxygenase-1 (HO-1) [44, 45]. HO-1 is a major antioxidant enzyme and exhibits anti-inflammatory properties by suppressing the release of pro-inflammatory cytokines, reactive oxygen species (ROS), and activation of NF- κ B p65 [46, 47]. Compound **5a** treatment increased the expression of HO-1 (Figure 3G) and consequently suppressed ROS production in BV-2 microglia (Figure 3H-I).

The anti-inflammatory effects of **5a** were also investigated in primary mouse astrocytes stimulated with LPS and interferon γ (IFN γ). Both **5a** and GW501516 exhibited no cytotoxicity in primary astrocytes up to 30 μ M (Figure S3A). Similar to the findings in BV-2 microglia, treatment with **5a** significantly reduced NO release by inhibiting the expression of NO synthase and suppressed the production of pro-inflammatory cytokines, including TNF- α , IL-1 β , and IL-6, in LPS/IFN γ -induced activated astrocytes (Figure S3B-E). These anti-inflammatory effects of **5a** on astrocytes were superior to those of GW501516 at the same concentration (Figure S3B-E). Taken together, these results indicate that **5a** potently downregulates inflammatory reactions in activated glial cells by reducing the levels of inflammatory mediators and NF- κ B signaling and promoting antioxidant activity.

5a prevents locomotor and cognitive deficits in the LPS-induced neuroinflammation model

To further investigate the anti-inflammatory effects of **5a** *in vivo*, neuroinflammation was induced by daily intraperitoneal injections of LPS (0.3 mg/kg per day) in mice. The mice were previously treated with **5a** (30 mg/kg per day, *p.o.*) for 4 days (Figure 4A). Chronic administration of LPS causes sickness and depression-like behavior such as decreased motor activity and anxiety symptoms, leading to impaired cognitive function [48-50]. We performed an open-field test to assess the exploratory behavior and locomotor activity of mice. LPS-treated mice showed a

decrease in total traveled distance and an increase in immobility time when compared with vehicle-treated mice (Figure 4B-D). The administration of compound 5a improved motor activity, which reached a level similar to that in vehicle-treated control mice (Figure

4B-D). In addition, 5a-administered mice spent more time in the center of the open field than LPS-treated mice, suggesting that LPS-induced anxiety was alleviated (Figure 4B,E).

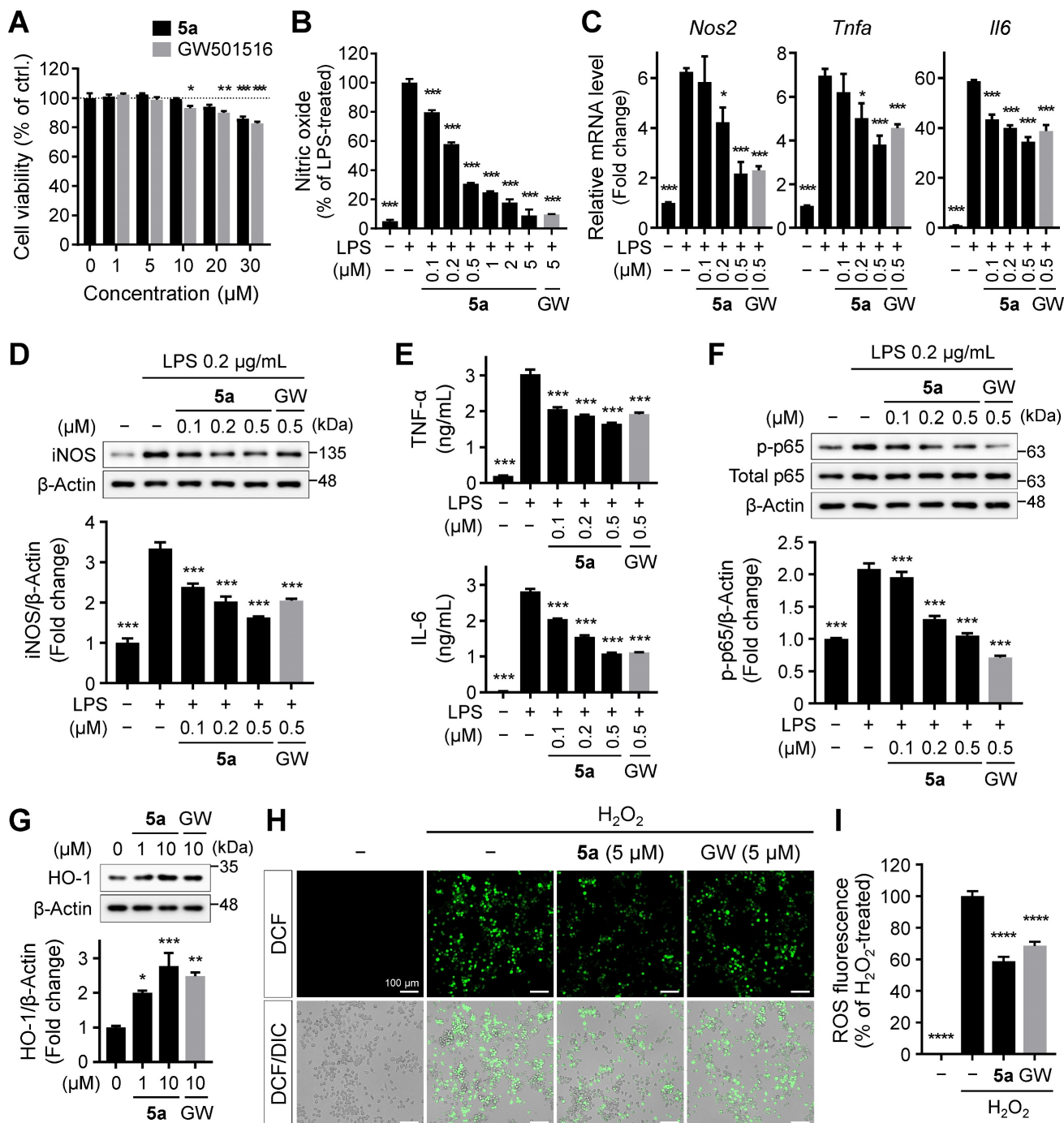


Figure 3. 5a reduces LPS-induced inflammatory responses in BV-2 microglia. (A) Viability of BV-2 microglial cells after treatment with 5a or GW501516 for 24 h. **P* < 0.05, ***P* < 0.01 and ****P* < 0.001 versus vehicle-treated control (one-way ANOVA with Dunnett's test). (B) Nitrite levels in the culture medium of BV-2 cells pretreated with 5a or GW501516 for 3 h followed by LPS (0.2 μg/mL) treatment for 24 h. (C) qRT-PCR analysis of relative mRNA expression of *Nos2* (*iNos*), *Tnfa*, and *Il6* in BV-2 cells pretreated with 5a or GW501516 for 12 h followed by LPS treatment for 3 h. *Hprt* mRNA levels were used to normalize the expression of each gene. (D) Western blot analysis for iNOS in BV-2 cells pretreated with 5a or GW501516 for 1 h followed by LPS treatment for 24 h. (E) TNF-α and IL-6 levels in the culture medium of BV-2 cells pretreated with 5a or GW501516 for 9 h followed by LPS treatment for 18 h. (F) Western blot analysis for phospho-NF-κB p65 (Ser536) and NF-κB p65 in BV-2 cells pretreated with 5a or GW501516 for 6 h followed by LPS treatment for 1 h. **P* < 0.05 and ****P* < 0.001 versus LPS-treated control (one-way ANOVA with Dunnett's test). (G) Western blot analysis for HO-1 in BV-2 cells after treatment with 5a or GW501516 for 48 h. **P* < 0.05, ***P* < 0.01 and ****P* < 0.001 versus vehicle-treated control (one-way ANOVA with Dunnett's test). (H-I) Intracellular ROS levels assessed via DCFH-DA staining. BV-2 cells were treated with 5a (5 μM) or GW501516 (5 μM) for 24 h followed by H₂O₂ (200 μM) for 20 min to induce oxidative stress. (H) Representative fluorescence images of DCFH-DA stained BV-2 cells. (I) Quantification of DCF fluorescence intensity in (H). *****P* < 0.0001 versus H₂O₂-treated control (one-way ANOVA with Dunnett's test). Data are presented as mean ± SEM. GW: GW501516.

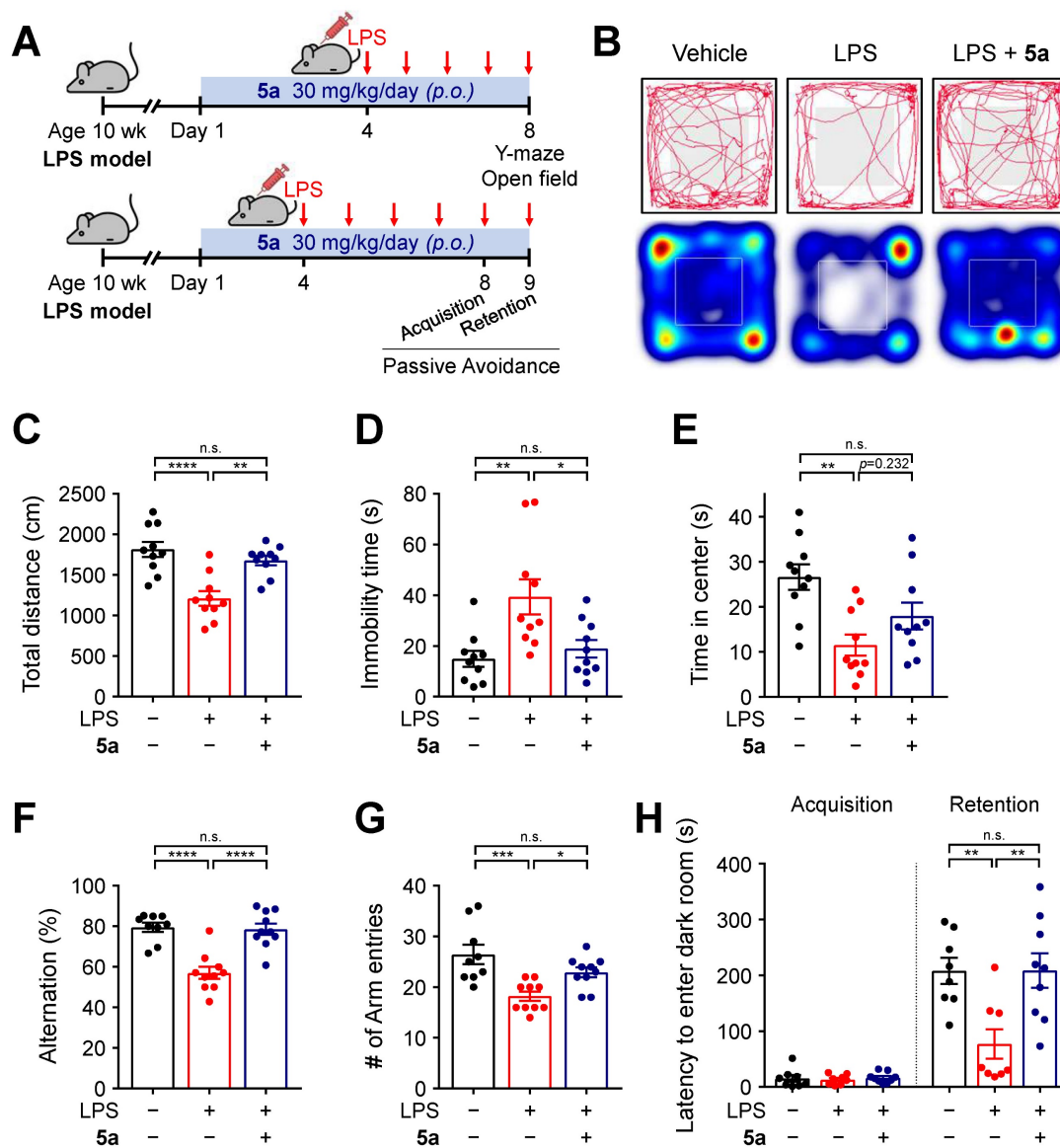


Figure 4. 5a reverses behavioral deficits in LPS-induced neuroinflammation. (A) Experimental protocol for behavioral tests after 5a administration (30 mg/kg/day, *p.o.*) in mice with LPS-induced neuroinflammation (0.3 mg/kg/day, *i.p.*). (B) Representative track plots (top) and heat maps (bottom) in the open-field test. The center zone is indicated by gray squares in the track plot or white outline squares in the heat map. (C–E) Total traveled distance (C), immobility time (D), and time spent in the center (E) in the open-field test ($n = 10$ mice per group). (F–G) Percentage of spontaneous alternation (F) and number of arm entries (G) in the Y-maze test ($n = 9–10$ mice per group). (H) Step-through latency to enter a dark room in the passive avoidance test ($n = 8–9$ mice per group). * $P < 0.05$, ** $P < 0.01$, *** $P < 0.001$ and **** $P < 0.0001$; n.s., not significant (one-way ANOVA with Tukey's test). Data are presented as mean \pm SEM.

We next examined the cognitive ability of mice by performing a Y-maze test and a passive avoidance test. In the Y-maze test, mice treated with 5a showed a higher percentage of spontaneous alternations reflecting better spatial learning and memory than LPS-treated mice (Figure 4F). 5a administration increased the number of arm entries, which was reduced in LPS-treated mice, consistent with the improvement in motor activity identified in the open-field test (Figure 4G). The passive avoidance test was conducted for assessing hippocampus-dependent contextual learning and memory performance. When compared with the vehicle-treated control, LPS-treated mice showed a reduced step-through

latency to enter the dark room owing to impaired memory (Figure 4H). However, administration of compound 5a significantly prevented this decrease (Figure 4H), indicating that 5a effectively restores cognitive deficits induced by LPS administration. Collectively, these results suggest that 5a counteracts inflammation-induced motor deficits and cognitive impairments *in vivo*.

Compound 5a ameliorates LPS-induced inflammation and glial activation *in vivo*

Next, we evaluated the *in vivo* protective effects of 5a against LPS-induced inflammation based on histological and biochemical analyses. C57BL/6N

mice were intraperitoneally injected with LPS 0.3 mg/kg for 7 days, with or without oral administration of **5a** 30 mg/kg for 10 days. Following repeated LPS injections, the spleens were enlarged compared to those of vehicle-treated mice. Administration of **5a** reduced the size and weight of spleens in the LPS-treated mice (Figure 5A-B). Compound **5a** also prevented the LPS-induced increases in the plasma levels of pro-inflammatory cytokines TNF- α and IL-6 (Figure 5C).

Systemic inflammation triggers immune responses in the CNS [51]. To determine whether **5a** treatment suppresses neuroinflammation and glial activation in the brain of mice, we immunostained the hippocampus and cortex regions with glial fibrillary acidic protein (GFAP) and ionized calcium-binding adaptor molecule 1 (IBA1), which are specific markers of astrocytes and microglia, respectively. Compared to the vehicle control, LPS increased the immunoreactivity for GFAP and IBA1 in both the hippocampus and cortex, and this effect was inhibited by **5a** (Figure 5D-F and Figure S4). We found that **5a** significantly reduced the expression of cluster of differentiation (CD)-86 (B7-2), a pro-inflammatory M1 marker, in IBA1-positive microglia compared with LPS-treated mice (Figure 5G-H). These results demonstrate that **5a** suppresses neuroinflammatory responses and glial activation induced by LPS.

Compound 5a restores learning and memory impairment in AD mice

To examine if PPAR δ agonist **5a** could alleviate AD-like pathology based on its anti-inflammatory properties, we investigated the therapeutic efficacy of **5a** using mice with scopolamine-induced cognitive impairment and 12-month-old APP^{swe}/PSEN1^{dE9} (APP/PS1) double transgenic mice. Compound **5a** was orally administered in a dosage of 30 mg/kg per day for 5 days, prior to scopolamine injection, in scopolamine-treated mice and for 10 days in APP/PS1 mice. We performed the Y-maze or passive avoidance test to assess learning and memory performance during the **5a** treatment period (Figure 6A and Figure S5A). On day 4 before the scopolamine injection (1 mg/kg, *i.p.*), the Y-maze test revealed no differences in the percentage of alternations and total number of arm entries between the mouse groups, indicating that they had normal cognitive function and motility before scopolamine injection (Figure S5B). We observed spatial working memory deficits in scopolamine-treated and APP/PS1 mice, as reflected by the significantly reduced percentage of spontaneous alternations compared to the vehicle-treated and wild-type (WT) mice, respectively (Figure 6B-C). Treatment with **5a** prevented the

decrease in alternation percentage in both AD models without inducing any changes in the total number of arm entries (Figure 6B-C). In the passive avoidance test, the scopolamine-treated mice showed a lower step-through latency than vehicle-treated mice, indicating cognitive decline; **5a** administration mitigated this effect (Figure S5C).

We further investigated the cognitive improvement efficacy of **5a** and GW501516 when post-administered in a dose-dependent manner using the scopolamine-treated mice (Figure S6A). In the Y-maze (Figure S6B), passive avoidance (Figure S6C), and Morris water maze test (Figure S6D-I), **5a** significantly restored the memory impairment in scopolamine-treated mice at a dose of 10 mg/kg and also showed maximum efficacy at a dose of 30 mg/kg, improving cognitive ability to a level similar to that of vehicle-treated mice, thereby confirming the dose-dependent therapeutic effects of **5a**. In addition, **5a** exhibited superior *in vivo* efficacy in improving cognitive function compared to GW501516 when administered at the same dose of 30 mg/kg (Figure S6B-I). Taken together, administration of **5a** effectively restores learning and memory impairment in mice with scopolamine-induced cognitive impairment and APP/PS1 mice.

Compound 5a mitigates reactive gliosis in APP/PS1 mice

Neuroinflammation accompanied by abnormal glial activation precedes neuropathological changes in AD and has been considered one of its pathogenic factors [29, 52]. Both reactive astrocytes and activated microglia secrete pro-inflammatory cytokines, chemokines, and ROS, resulting in neurotoxicity [28, 53]. Thus, we investigated whether treatment with **5a** interferes with neuroinflammation by regulating the activation of glial cells in AD mice. Compared with age-matched WT littermates, the APP/PS1 mice showed markedly increased immunoreactivity for GFAP and IBA1 in the molecular layer of the dentate gyrus (Figure 6D-E). The excessive glial activity was significantly inhibited by **5a** treatment (Figure 6D-E). APP/PS1 mice treated with **5a** also exhibited reduced levels of mRNA expression of *Gfap* in hippocampus homogenates, compared with the vehicle-treated APP/PS1 mice (Figure 6F). Additionally, Sholl analysis was performed to investigate the morphological characteristics of astrocytes and quantify the size and complexity of astrocytic processes, including maximum process lengths, sum of process intersections, and number of branch points. When compared with the astrocytes in WT mice, astrocytes in APP/PS1 mice were hypertrophied, as confirmed by a higher ending radius, sum of

intersections, and ramification index (Figure 6G-H). In contrast, **5a** treatment significantly suppressed the astrocytic hypertrophy in APP/PS1 mice (Figure

6G-H). These results indicate that **5a** attenuates AD-like dysregulations including neuroinflammation and reactive gliosis in AD mice.

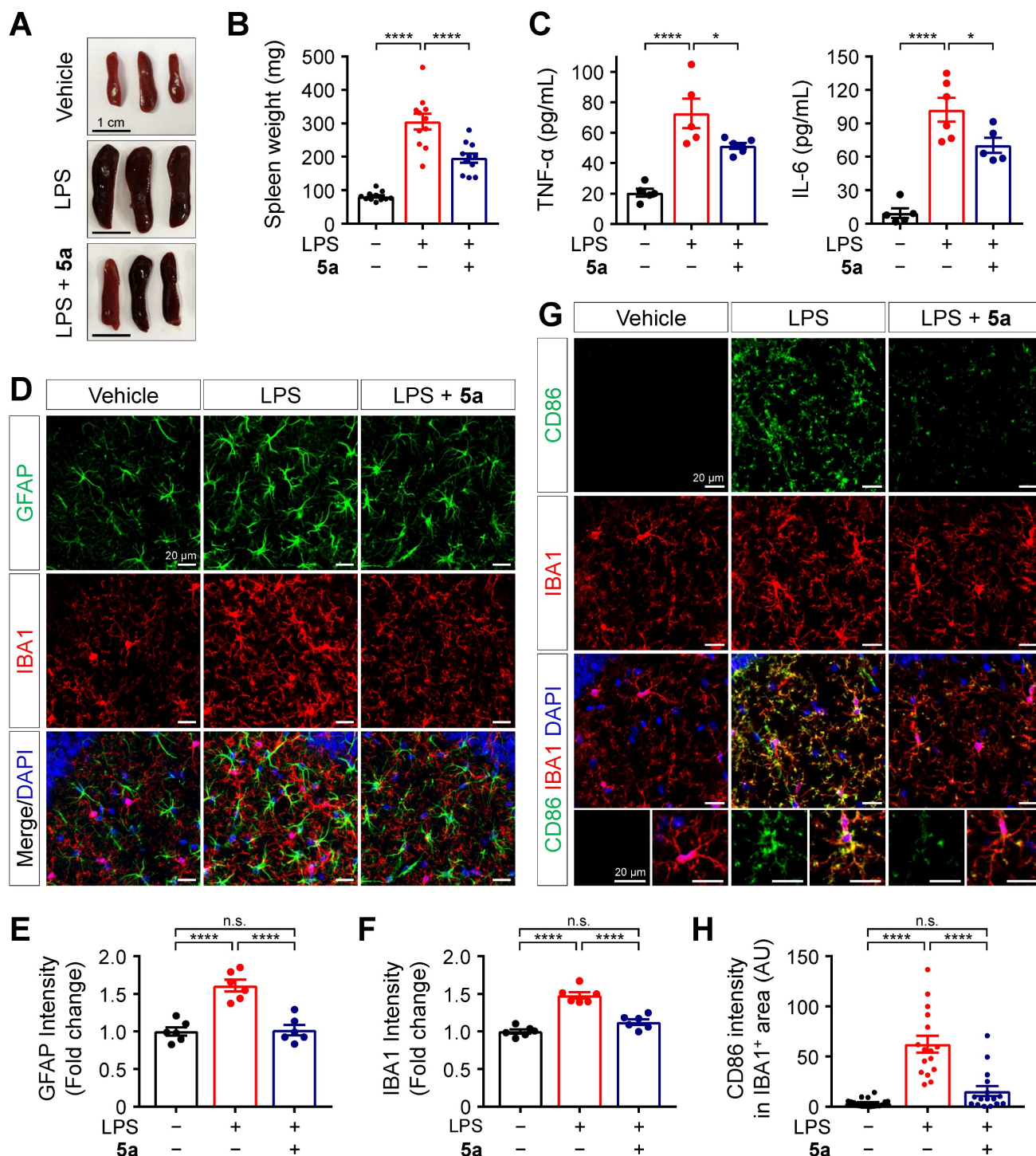


Figure 5. **5a** prevents LPS-induced inflammation and glial activation. **(A-B)** Representative images **(A)** and mean weight **(B)** of dissected spleens from vehicle- and LPS-treated mice (0.3 mg/kg/day for 7 days, *i.p.*) with or without oral administrations of **5a** (30 mg/kg/day for 10 days) ($n = 11$ mice per group). **(C)** Plasma cytokine levels in vehicle- and LPS-treated mice with or without oral administrations of **5a** ($n = 5-6$ mice per group). * $P < 0.05$, and **** $P < 0.0001$ (one-way ANOVA with Dunnett's test). **(D)** Representative immunofluorescence images showing GFAP (green) and IBA1 (red) in CA1 region of hippocampus. **(E-F)** Quantification of immunoreactivity for GFAP **(E)** and IBA1 **(F)** in **(D)** ($n = 6$ brain sections from six mice per group). **(G)** Representative immunofluorescence images showing CD86 (green) and IBA1 (red) in the CA1 hippocampal region. **(H)** Mean intensity of CD86 in IBA1-positive areas ($n = 16-18$ brain sections from six mice per group). **** $P < 0.0001$; n.s., not significant (one-way ANOVA with Tukey's test). Data are presented as mean \pm SEM.

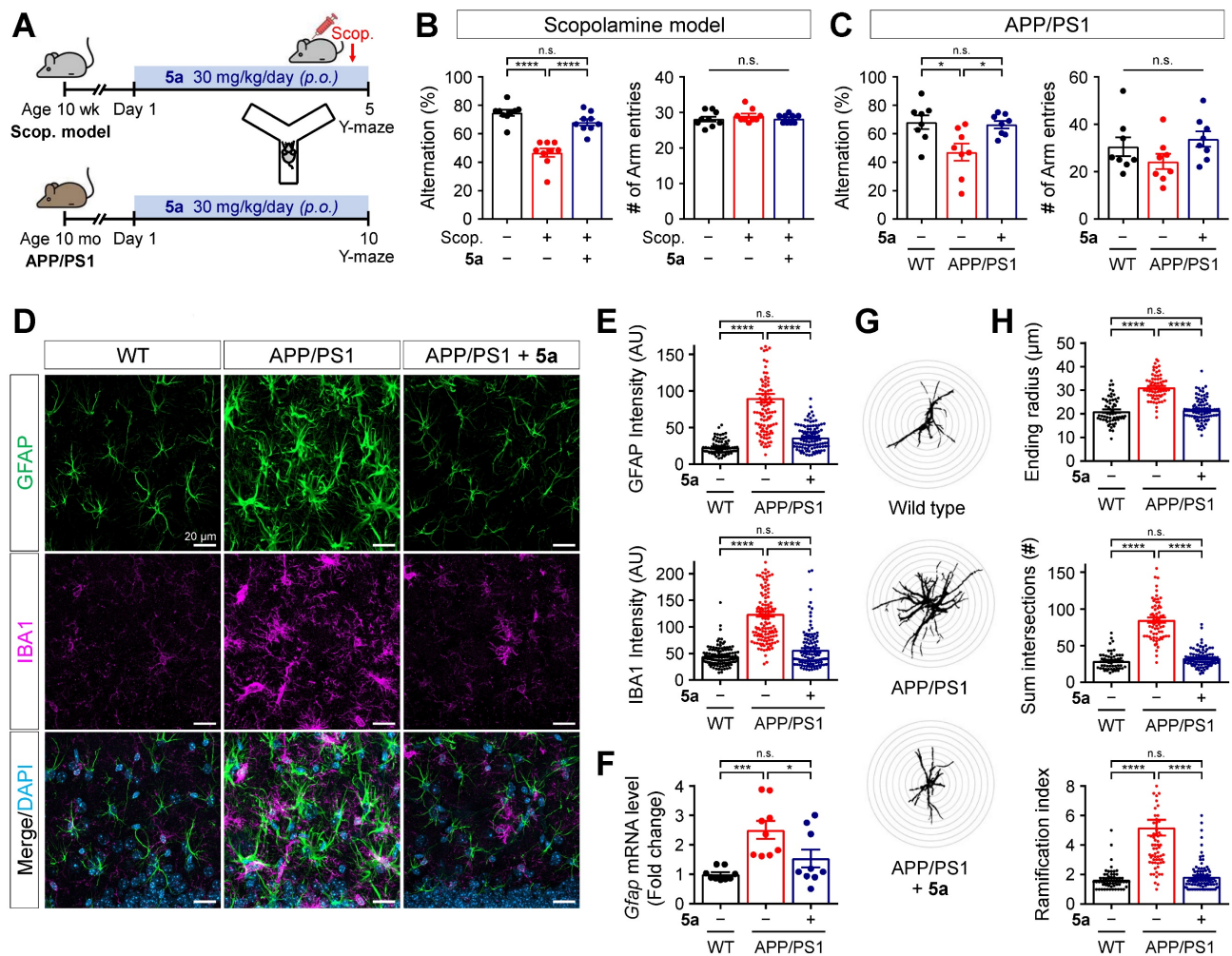


Figure 6. 5a ameliorates cognitive impairment and AD-like features in mice with AD. (A) Experimental protocol for the Y-maze test after oral administration of 5a in mice with scopolamine-induced cognitive impairment (n = 9 mice per group) or APP/PS1 mice (n = 8 mice per group). (B–C) Percentage of spontaneous alternations (left) and number of arm entries (right) for mice with scopolamine-induced cognitive impairment (B) or APP/PS1 mice (C) treated with vehicle or 5a in the Y-maze test. (D) Representative immunofluorescence images showing GFAP (green) and IBA1 (magenta) in the hippocampal dentate gyrus of WT and APP/PS1 mice treated with vehicle or 5a (n = 8 brain sections from four mice per group). (E) Quantification of immunoreactivity for GFAP (top) and IBA1 (bottom) in (D). (F) Relative mRNA expression of *Gfap* in the hippocampus of WT and APP/PS1 mice treated with vehicle or 5a (n = 9 mice per group). *Hprt* mRNA levels were used to normalize *Gfap* expression. (G) Representative images of Sholl analysis for GFAP-positive astrocytes in the hippocampal dentate gyrus of WT and APP/PS1 mice treated with vehicle or 5a (n = 59–90 astrocytes in 8 brain sections from four mice per group). (H) Quantification of ending radius (top), sum of intersections (middle), and ramification index (bottom) of GFAP-positive astrocytes by Sholl analysis. *P < 0.05, ***P < 0.001 and ****P < 0.0001; n.s., not significant (one-way ANOVA with Tukey’s test). Data are presented as mean ± SEM. Scop.: scopolamine; AU: arbitrary unit.

5a reduces amyloid burden by inhibiting beta-secretase 1 (BACE1) expression in APP/PS1 mice

According to a previous study, PPARδ activation reduces the expression of BACE1 responsible for Aβ production in SH-SY5Y neuroblastoma cells [54]. We also confirmed that 5a dose-dependently reduced the expression of BACE1 in SH-SY5Y cells (Figure 7A–B). We next investigated whether 5a-induced PPARδ activation inhibits beta-amyloid production in a mouse model of AD. Consistent with the results obtained following *in vitro* assessment, BACE1 levels were significantly diminished in cortical homogenates of 5a-treated APP/PS1 mice compared to those in vehicle-treated APP/PS1 mice (Figure 7C–D). To examine whether 5a could ameliorate the Aβ deposition in the brain, one of the major pathological

features of AD, we performed thioflavin-S staining of brain tissues collected from WT and APP/PS1 mice treated with vehicle or 5a and quantified the number and area of plaques in the cortex or hippocampus. Aβ plaques accumulated in the entire cortical and hippocampal region of 10-month-old APP/PS1 mice, whereas no Aβ plaques were detected in WT mice. (Figure 7E–F). Compared with vehicle-treated APP/PS1 mice, 5a-treated APP/PS1 mice showed a significant reduction in the number and area of Aβ plaques in both the cortex and hippocampus, indicating that 5a effectively reduced amyloid burden in APP/PS1 mice (Figure 7E–F).

In transgenic mouse models and patients with AD, BACE1-induced Aβ deposition subsequently causes BACE1 accumulation in neurons around amyloid plaques, leading to a positive-feedback loop

in the amyloidogenic pathway [55-57]. We observed that BACE1 was highly expressed around 6E10-positive amyloid plaques in association with overall A β accumulation in the hippocampus of APP/PS1 mice (Figure 7G-H). In contrast, **5a** administration significantly reduced the plaque-associated BACE1 accumulation in APP/PS1 mice (Figure 7G-H). Collectively, these results indicate that **5a** ameliorates amyloid-related pathology through BACE1 inhibition following PPAR δ activation in APP/PS1 mice.

Additionally, we investigated whether PPAR δ activation with **5a** could alleviate tau pathology,

another pathological hallmark of AD. In mouse models of β -amyloidosis, although neurofibrillary tangles are not observed, hyperphosphorylation of tau occurs within dystrophic neurites surrounding amyloid plaques [58, 59]. APP/PS1 mice treated with **5a** tend to decrease AT8-positive phosphorylated tau around thioflavin S-positive A β plaques, although this was insignificant (Figure S7A-B). However, **5a** treatment reduced the amount of amyloid plaques and their associated phosphorylated tau, thereby inhibiting overall tau hyperphosphorylation in the brain (Figure S7C-E).

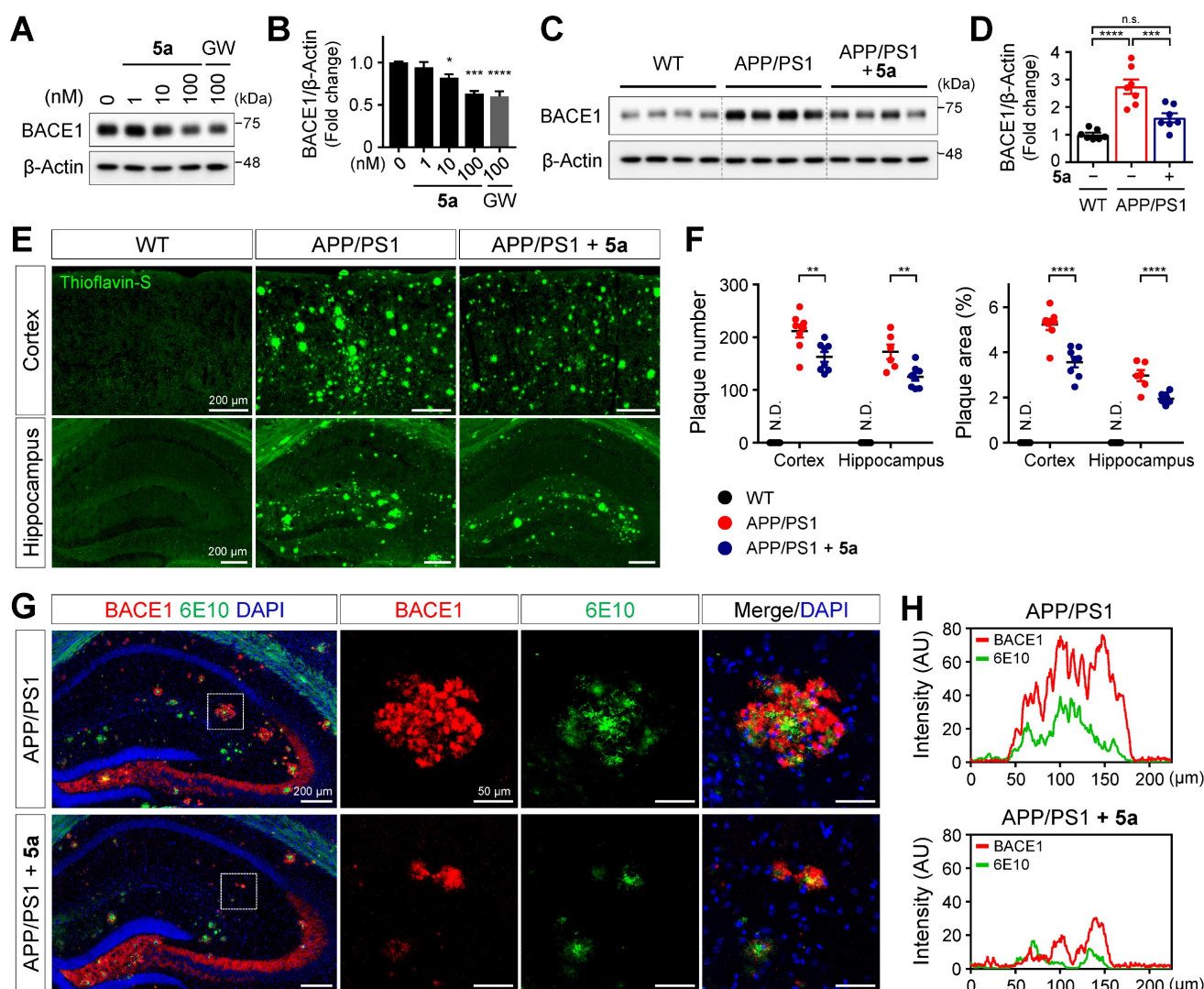


Figure 7. **5a** reduces BACE1 expression and amyloid burden in APP/PS1 mice. **(A-B)** Western blot analysis for BACE1 in SH-SY5Y cells after treatment with **5a** or GW501516 for 24 h. * $P < 0.05$, *** $P < 0.001$ and **** $P < 0.0001$ versus vehicle-treated control (one-way ANOVA with Dunnett's test). **(C-D)** Western blot analysis for BACE1 in cortical homogenates of WT and APP/PS1 mice treated with vehicle or **5a** ($n = 7$ mice per group). **(E)** Thioflavin-S staining for A β plaques in the cortex and hippocampus of WT and APP/PS1 mice treated with vehicle or **5a** ($n = 8$ brain sections from four mice per group). **(F)** The number (left) and area (right) of thioflavin-S-stained A β plaques in the cortex and hippocampus. ** $P < 0.01$, *** $P < 0.001$ and **** $P < 0.0001$; n.s., not significant (one-way ANOVA with Tukey's test). **(G)** Immunoreactivity of BACE1 (red) around 6E10 (green)-positive amyloid plaque in the hippocampus of APP/PS1 mice treated with vehicle or **5a** ($n = 4$ brain sections from four mice per group). Right, higher-magnification images of the dotted boxed area in the hippocampus. **(H)** Intensity profile plots showing colocalization of BACE1 with 6E10 in APP/PS1 mice treated with vehicle (top) or **5a** (bottom) were measured using the magnified images in (G). Data are presented as mean \pm SEM. N.D.: not detected; AU: arbitrary unit.

Discussion

In the present study, we designed a straightforward three-step approach to synthesize novel PPAR δ -selective agonists with a selenazole heterocyclic core using commercially available 4-iodo-2-methylphenol. Compound **5a** was the most potent and selective PPAR δ agonist with optimal *in vitro* ADMET and *in vivo* PK profiles. We determined the binding mode of **5a** to hPPAR δ through an X-ray crystallographic analysis of the ligand-hPPAR δ complex. Compound **5a** induced transcriptional activation of representative PPAR δ target genes, including pyruvate dehydrogenase kinase 4 (*Pdk4*), angiopoietin-like 4 (*Angptl4*), and *Cd36*, confirming its effects on PPAR δ activation *in vitro* and *in vivo* (Figure S8). We confirmed that **5a** inhibits excessive inflammatory responses in activated glial cells. Consistent with *in vitro* efficacy, **5a** treatment suppressed inflammatory responses and ameliorated behavioral defects in mice with LPS-induced neuroinflammation. The administration of **5a** also prevented glial hyperactivation and A β accumulation and subsequently restored learning and memory deficits in AD mice, suggesting its potential therapeutic applications for this pathology.

Although among other PPAR subtypes, PPAR δ is the most abundantly expressed in the brain [8-10], its functional role in the CNS has been rarely studied, compared to PPAR α or PPAR γ . The role of PPAR δ in inflammation and neurodegeneration is not fully understood owing to a lack of PPAR δ -specific agonists [15]. In our functional activity assay, **5a** showed a highly potent and specific agonistic effect on PPAR δ with over 14,000-fold selectivity over PPAR α and PPAR γ . This PPAR δ -selective agonist could be used for in-depth exploration to clarify PPAR δ actions in the CNS.

Despite numerous efforts over decades, the development of effective treatments for AD remains a challenge. The AD drugs approved by the FDA so far have a limited efficacy, offering only symptomatic relief along with several side effects, and demonstrate short-term or questionable efficacy for cognitive improvement; similar concerns are observed with the currently approved amyloid-targeting antibodies [27, 60]. AD is a complex degenerative disease that progresses over a long period of time and is caused by the interaction of multiple pathological pathways [28, 29]. Therefore, overall targeting of these AD-related mechanisms, including neuroinflammation, nitrosative or oxidative stress, and reactive gliosis, could be an attractive therapeutic strategy in AD. In this study, we developed a novel PPAR δ agonist **5a** and found that it is a potent anti-inflammatory agent

that suppresses the expression of pro-inflammatory cytokines, NF- κ B activation, and glial reactivity *in vitro* and *in vivo*. Compound **5a** reduces nitrosative stress by inhibition of iNOS and functions as an antioxidant, decreasing ROS accumulation owing to the induction of the antioxidant enzyme HO-1. These results support the beneficial effects of **5a** on multiple pathogenic pathways in AD.

PPARs regulate inflammation and immunity primarily through transrepression of other transcriptional factors such as NF- κ B, signal transducers and activators of transcription (STATs), and activator protein 1 (AP1). Thus, their activation functionally antagonizes downstream signaling cascades [15]. PPAR δ regulates inflammatory responses by inhibiting NF- κ B [61, 62], JAK2/STAT1 [54, 63], and STAT3 signaling [62], resulting in reduced levels of iNOS, pro-inflammatory cytokines, chemokines, and vascular cell adhesion molecule 1 (VCAM1). PPAR δ -deficient mice showed cognitive impairment associated with increased cytokine levels, NF- κ B activation, and astrogliosis [32]. These findings indicate that PPAR δ has a crucial role in inflammation control, and a correlation exists between severe neuroinflammation and cognitive deficits. PPAR δ activation with agonists such as GW0742 or GW501516 inhibits cytokine expression, ROS production, and inflammasome activation *in vitro*, in LPS-stimulated adipocytes [61] and brain cells [63, 64], and *in vivo*, as observed in the lung [65], heart [62], and liver [66] tissues of LPS-treated mice. In this study, we provide the first evidence for protective effects of **5a**-mediated PPAR δ activation against cognitive decline accompanied by neuroinflammation. These effects include the amelioration of locomotor impairments, cognitive deficits, and glial reactivity induced by chronic LPS administration in mice.

Recent findings indicate that PPAR δ is involved in the pathogenesis of AD [16-18]. PPAR δ agonists have previously shown therapeutic efficacy against AD-like pathologies in A β ₁₋₄₂-infused [31] or 5XFAD transgenic mouse models of AD [34], primarily through their anti-inflammatory effects. Interestingly, PPAR δ deficiency was reported to accelerate tau hyperphosphorylation and amyloidogenesis, two pathological hallmarks of AD [32]. PPAR δ -null mice showed increased levels of BACE1, which is responsible for A β production, in the cortex [32]. The peroxisome proliferator response element (PPRE), the binding site of all PPARs after activation, is present in the BACE1 promoter and PPAR γ represses BACE1 transcription by direct binding to this PPRE [67]. Ligand-activated PPAR δ binds to the PPRE in the promoter region of suppressor of cytokine signaling 1

(SOCS1) rather than that of BACE1, thereby suppressing BACE1 expression through SOCS1-mediated inhibition of STAT1 signaling in SH-SY5Y cells [54]. Herein, we report for the first time that PPAR δ activation following administration of **5a** reduces BACE1 expression in the brain of APP/PS1 mice of AD. Further studies are still required to elucidate the precise mechanisms by which PPAR δ regulation is involved in BACE1 transcription during APP processing in AD.

Hyperactivated microglia release inflammatory factors, causing neuroinflammation and worsening the progression of AD. However, before turning into a detrimental state under inflammatory and pathological conditions, microglia play a neuroprotective role by A β phagocytosis in the initial stage of AD [68, 69]. PPAR δ has been reported to be involved in apoptotic cell clearance by inducing opsonin genes in macrophages [70]. In the 5xFAD mouse model of AD, pharmacological activation of PPAR δ increases microglial association around A β plaques [34]. We also observed a significant increase in the number of microglia per plaque in **5a**-treated APP/PS1 mice, indicating enhanced microglial recruitment to A β plaques (Figure S9A-B). In addition, **5a** treatment increased the phagolysosome area within plaque-associated microglia (Figure S9A, C) and the internalized A β area within the phagolysosome (Figure S9A, D), suggesting that activation of PPAR δ with **5a** enhances microglial phagocytosis and contributes to A β clearance. Further studies are needed to investigate the underlying mechanisms of PPAR δ -mediated regulation on microglial phagocytosis.

In conclusion, PPAR δ activation with **5a** leads to favorable effects on amyloid burden via multiple mechanisms that inhibit excessive inflammation, oxidative stress, and increased levels of BACE1, which are all risk factors for A β deposition, thereby restoring cognitive impairment in the mouse models of AD. Our findings demonstrate that a selective PPAR δ agonist **5a** could be investigated as a drug candidate for AD treatment.

Materials and Methods

General synthetic method

All reactions were performed in oven- and flame-dried glassware under a nitrogen (N $_2$) atmosphere. Air- and moisture-sensitive reagents and solvents were transferred via syringes or cannulae into the reaction vessel through a rubber septum. Chemicals were obtained from commercial sources and used without further purification. Flash column chromatography was carried out using silica gel

(particle size 230–400 mesh). Analytical thin-layer chromatography (TLC) was performed using silica gel 60 F254. TLC plates were visualized with UV light, by staining with 5% ammonium dimolybdate or panisaldehyde in ethanol and applying heat. ^1H nuclear magnetic resonance (NMR, 300, 400, and 600 MHz) and ^{13}C NMR (75 and 150 MHz) spectra were recorded for solutions in CDCl $_3$ and MeOH-*d* $_4$. Chemical shifts (δ) are expressed in parts per million (ppm) downfield from the internal reference, tetramethylsilane, or from residual CHCl $_3$ in CDCl $_3$. The purity of compounds was analyzed using high-performance liquid chromatography/mass spectrometry (HPLC/MS) spectra; mass spectrometry was conducted in positive electrospray ionization (ESI) mode on an LCMS-2020 system (Shimadzu). Column chromatography was performed using a CombiFlash $^{\text{®}}$ Rf system with Re-diSep $^{\text{®}}$ Rf (Teledyne ISCO). For the final compounds, further purification was performed by preparative HPLC on Kinetex $^{\text{®}}$ 5 μm Biphenyl 100 \AA (GX-281 HPLC system, Gilson; column tube: 250 mm \times 21.2 mm ID) using ACN/H $_2$ O as eluent. The purity of target compounds was determined to be > 95% by analytical HPLC using a dual different wavelength UV detector. Starting materials were obtained from Sigma-Aldrich (St. Louis, MO, USA), or Alfa Aesar (Ward Hill, MA, USA). Solvents were obtained from Fisher Scientific (Hampton, NH, USA) or Sigma-Aldrich and were used without further purification unless noted otherwise.

{2-Methyl-4-[4-methyl-2-(4-trifluoromethyl-phenyl)-selenazol-5-yl-methylsulfanyl]-phenoxy}-acetic acid (**5a**)

LiOH (0.6 mL solution 2 M [1.2 mmol]) was slowly added to a stirred solution of **4a** (528 mg, 1.0 mmol) in 15 mL tetrahydrofuran (THF) and 10 mL H $_2$ O at 0 $^{\circ}\text{C}$. The reaction mixture was stirred at 0 $^{\circ}\text{C}$ until TLC indicated the completion of the reaction (approximately 2 h). The mixture was then diluted with water (10 mL), acidified with 0.5 M NaHSO $_4$ (2.5 mL), and extracted with a mixed solvent containing EtOAc and THF (3:1, 15 mL). The organic layers were combined, dried (on Na $_2$ SO $_4$), and concentrated. The residue was purified by column chromatography on silica gel with CH $_2$ Cl $_2$ /MeOH (10:1) and **5a** was obtained as a white solid (460 mg, 92%). ^1H NMR (600 MHz, MeOH-*d* $_4$) δ : 7.95 (d, 2 H, J = 8.2 Hz), 7.70 (d, 2 H, J = 8.3 Hz), 7.19–7.17 (m, 2 H), 6.71 (d, 1 H, J = 8.4 Hz), 4.55 (s, 2 H), 4.22 (s, 2 H), 2.20 (s, 3 H), 2.15 (s, 3 H). ^{13}C NMR (150 MHz, MeOH-*d* $_4$) δ : 171.4, 158.4, 152.4, 151.6, 140.9, 140.8, 137.0, 133.4, 129.3, 128.1, 127.2, 125.8, 112.9, 67.4, 35.2, 16.5, 15.4. LC/MS (ESI $^+$) calculated for C $_{21}$ H $_{18}$ F $_3$ NO $_3$ Se

identified as $[M + H]^+$ ion as m/z 500.39. Found: m/z 502.03 (isotope).

{2-Methyl-4-[4-methyl-2-(4-trifluoromethyl-phenyl)-selenazol-5-yl-methylselenanyl]-phenoxy}-acetic acid (5b)

LiOH (0.6 mL solution of concentration 2 M [1.2 mmol]) was slowly added to a stirred solution of 4b (575 mg, 1.0 mmol) in 15 mL THF and 10 mL H₂O at 0 °C. The reaction mixture was stirred at 0 °C until TLC indicated the completion of the reaction (approximately 2 h). The mixture was then diluted with water (10 mL), acidified with 0.5 M NaHSO₄ (2.5 mL), and extracted with a mixed solvent containing EtOAc and THF (3:1, 15 mL). The organic layers were combined, dried (on Na₂SO₄), and concentrated. The residue was purified by column chromatography on silica gel with CH₂Cl₂/MeOH (10:1) and 5b was obtained as a white solid (492 mg, 90%). ¹H NMR (600 MHz, CDCl₃) δ: 7.87 (d, 2 H, *J* = 8.1 Hz), 7.62 (d, 2 H, *J* = 8.2 Hz), 7.30 (s, 1 H), 7.22 (d, 1 H, *J* = 8.3 Hz), 6.55 (d, 1 H, *J* = 8.4 Hz), 4.59 (s, 2 H), 4.17 (s, 2 H), 2.20 (s, 3 H), 2.08 (s, 3 H). ¹³C NMR (150 MHz, CDCl₃) δ: 173.4, 169.6, 156.5, 151.4, 139.2, 138.4, 133.4, 128.6, 127.1, 126.2, 123.2, 120.2, 112.0, 65.5, 25.6, 16.2, 15.3. LC/MS (ESI⁺) calculated for C₂₁H₁₈F₃NO₃Se₂ identified as $[M + H]^+$ at m/z 547.29. Found: m/z 550.00 (isotope).

Protein production and crystallization

A human recombinant DNA PPARδ LBD (residues 171 – 441) was designed. Following codon optimization, it was inserted into a pET28a vector. N-terminal 6 His-tagged Human PPARδ LBD (171–441) was overexpressed in *Escherichia coli* BL21-Star (DE3) cells. The cells were grown at 37 °C to an optical density at 600 nm (OD₆₀₀) of 1.0 in Terrific Broth (TB) medium containing 50 µg/mL kanamycin and induced with 0.5 mM isopropyl-β-D-thiogalactopyranoside (IPTG). Inclusion bodies formed by the overexpressed proteins were studied 16 h after IPTG induction at 18 °C, followed by harvesting using centrifugation at 6000 rpm and 4 °C for 15 min. The cell pellets were resuspended in lysis buffer (50 mM Bis-Tris propane pH 8.5, 500 mM NaCl, 10% glycerol, and 5 mM β-mercaptoethanol) and lysed in an ultrasonic processor. The cell lysate was centrifuged at 15,000 rpm for 40 min at 4 °C. N-terminal His-tagged Human PPARδ LBD in the supernatant fraction was purified via nickel affinity chromatography followed by gel filtration. The protein was concentrated to 8 mg/mL in 20 mM HEPES (final pH 7.5), 500 mM ammonium acetate, and 10 mM β-mercaptoethanol for crystallization. Crystallization was carried out using the

hanging-drop vapor diffusion method. Apo crystals of human PPARδ LBD were obtained from a 4 µL drop consisting of 2 µL well solution [5 – 15% (w/v) PEG 8000, 40 mM Bis-tris propane pH 7.0 – 9.5, 2.5% 1,2-propanediol, 200 mM KCl, and 10 mM dithiothreitol (DTT)] and 2 µL of protein, with 10% n-Hexyl-β-D-glucopyranoside 1 M. The crystals appeared within 2–3 days. The co-crystal complex-5a was obtained by soaking the apo crystal in 250 µM selenazole for 24 h in the presence of 10% PEG 8000, 40 mM Bis-tris propane (pH 8.5), 2.5% 1,2-propanediol, 200 mM KCl, and 10 mM DTT at 18 °C. For the diffraction test, crystals were cryo-protected by dipping into a solution of 10% PEG 8000, 40 mM Bis-tris-propane (pH 8.5), 2.5% 1,2-propanediol, 200 mM KCl, 10 mM DTT, and 20% glycerol (v/v).

Data collection, structure determination, and refinement

Diffraction data were collected at 1.70 Å resolution, using in-vacuum undulator beamline BL-5C of the Pohang Accelerator Laboratory (PAL), South Korea. HKL2000 (HKL Research, Inc.) was used for integration and scaling. Molecular replacement was used to determine the structure of human PPARδ LBD bound with 5a using a previously known human PPARδ LBD structure (PDB entry: 5U3R) without water and ligand, as a search model. Rigid body refinement, followed by simulated annealing at 5000 K, was conducted using PHENIX (Python-based Hierarchical ENvironment for Integrated Xtallography). Subsequently, refinement was conducted in alternating cycles of manual model building in COOT (Crystallographic Object-Oriented Toolkit), followed by restrained refinement in PHENIX until the R factors converged. Data collection and refinement statistics are shown in Table S5. The coordinate and structural factors of the complex structure have been deposited in the Protein Data Bank (PDB code: 5Y7X). Structure visualization was performed with Chimera [71].

CYP inhibition assay

All incubations were performed in duplicate, and the mean values were used for analysis. Cocktail incubations were carried out using eight probe substrates of CYP1A2, CYP2C9, CYP2C19, CYP2D6, and CYP3A4: phenacetin, tolbutamide, mephenytoin, dextromethorphan and midazolam respectively, followed by tandem mass spectrometry. Briefly, an incubation reaction was performed using 0.25 mg/mL human liver microsomes in a final incubation volume of 100 µL. The incubation medium contained 100 mM phosphate buffer (pH 7.4) and probe substrates. The

incubation mixture containing various inhibitors (10 μM) was pre-incubated for 5 min. After pre-incubation, an NADPH-regenerating system was added. After incubation at 37 $^{\circ}\text{C}$ for 15 min, the reaction was stopped by placing the incubation tubes on ice and adding 40 μL of ice-cold acetonitrile. The incubation mixtures were centrifuged at 10,000 g and 4 $^{\circ}\text{C}$ for 5 min. Aliquots of the supernatant were injected onto an LC-MS/MS system. The CYP-mediated activities in the presence of inhibitors were expressed as a percentage of the corresponding control value [72].

Metabolic stability assay in liver microsomes

The metabolic stability assay was performed by incubation of human and selected animal liver microsomes (dog, rat, and mouse) with the test compound at a final concentration of 1 μM , in the presence of 0.5 mg/ml microsomal protein and NADPH-regeneration system, in a total volume of 100 μL phosphate buffer 100 mM (pH 7.4) at 37 $^{\circ}\text{C}$. The incubation was started by introducing the NADPH-regeneration system and terminated by adding 40 μL of ice-cold acetonitrile at 0- and 30 min. Precipitated proteins were removed by centrifugation at 10,000 g and 4 $^{\circ}\text{C}$ for 5 min. Aliquots of the supernatant were injected onto an LC-MS/MS system. Incubations terminated prior to addition of the NADPH-regeneration system (time point, 0 min) were used as standards, defined as 100%. Percent of the parent compound remaining was calculated by comparing peak areas [73].

hERG channel inhibition assay

An hERG channel binding assay was performed using the Predictor hERG Fluorescence Polarization Assay Kit (PV5365, Invitrogen). Briefly, for measuring IC_{50} , compounds were serially diluted (16 points, 3-fold) and then mixed for 4 h at 25 $^{\circ}\text{C}$ with a reaction mixture containing hERG membrane, fluorescence tracer red dye, and fluorescence polarization buffer. Fluorescence intensity (excitation at 530 nm, emission at 590 nm) was measured using a multi-mode microplate reader Synergy Neo (Biotek). E-4031 was used as the reference positive standard (IC_{50} = 10 – 90 nM) [74].

Pharmacokinetics studies

Sprague-Dawley rats (weighing 250–300 g, 7-week-old) were fasted for 16 h and used for experiments. Before administration of compound **5a**, blood was collected from the jugular vein and used as a blank control. For oral administration, four rats received the compound suspended in 10% DMSO, 15% water, and 75% PEG 400 at a dose of 10 mg/kg via oral gavage. For intravenous administration, a

dose of 1 mg/kg of the compound was injected into the caudal vein. The volumes of administration were 600 μL for oral and 200 μL for intravenous administration. Blood from the jugular vein was collected into a heparinized tube at 0.08, 0.25, 0.5, 1, 2, 4, 6, and 8 h after compound administration. Plasma samples were prepared from the extracted blood by centrifugation at 12,000 rpm for 15 min. Then, 20 μL of plasma was mixed with 80 μL of acetonitrile containing internal standard and centrifuged at 14,000 rpm for 5 min. Collected plasma supernatants were loaded into triple quadrupole LC-MS/MS (Triple Quad 5500, Applied Biosystems) and the amount of contained compound was measured. The calibration curve had a range of 5 to 1000 ng/mL, and the lower limit of quantification was 5 ng/mL. Non-compartmental analysis was used to determine pharmacokinetic parameters (Phoenix WinNolin ver 6.4, Pharsight).

Ames MPF mutagenicity assay

An Ames microplate format (MPF) 98/100 mutagenesis assay kit (Xenometrix) was used to test mutagenic activity. The TA98 / TA100 *Salmonella* strain was inoculated into the bacterial culture medium and cultured overnight. The *Salmonella* test strain was then exposed to six concentrations of the test compound (plus positive and negative controls). Samples were prepared in 96-well plates in sterile DMSO. The cultured bacteria, test compound, and S9 mixture were incubated for 90 min at 37 $^{\circ}\text{C}$ in a shaking incubator. The mixture was then treated with an indicator medium and dispensed into 384-well plates. The plates were incubated at 37 $^{\circ}\text{C}$ for 48 h. The number of wells containing revertant colonies was counted for each dose.

Cell culture

For the *in vitro* co-transfection assay, CV-1 monkey kidney cells were cultured in Dulbecco's modified Eagle's medium (DMEM) supplemented with 10% resin-charcoal-stripped fetal bovine serum (FBS), 100 U/mL penicillin, and 100 g/mL streptomycin. To investigate the anti-inflammatory effects of **5a**, BV-2 microglial cells were cultured in RPMI 1640 (Biowest) supplemented with 10% heat-inactivated FBS (Biowest), 2.05 mM L-glutamine (Gibco), and 100 U/mL penicillin/streptomycin (Gibco). Primary mouse astrocytes were isolated from postnatal day 1 C57BL/6N mouse pups. The cerebral cortices collected with the meninges removed were triturated by gentle pipetting and centrifuged. Primary astrocytes were resuspended and cultured in DMEM supplemented with 10% heat-inactivated FBS (Biowest), 10% heat-inactivated horse serum (Gibco),

and 100 U/mL penicillin/streptomycin (Gibco). On days *in vitro* (DIV) 4, floating other cell types were removed by tapping the culture dish, and astrocytes were used for experiments on DIV6. To investigate the effects of **5a** on BACE1 expression, SH-SY5Y human neuroblastoma cells (Korean Cell Line Bank, 22266) were cultured in minimum essential medium (MEM) supplemented with 10% heat-inactivated FBS (Biowest), 25 mM HEPES (Gibco), 25 mM sodium bicarbonate (Gibco) and 100 U/mL penicillin/streptomycin (Gibco). Cells were maintained at 37 °C in a humidified atmosphere containing 5% CO₂.

In vitro transfection assay

CV-1 cells were seeded at 6×10^3 cells per well in 96-well culture plates and transfected once they reached 70% confluency. The cells were washed with serum-free medium and then transfected with a plasmid mixture containing human PPAR expression vector, β -galactosidase, and TK-PPRE-Luc vector by Superfecta reagent (QIAGEN). Twenty-four hours post-transfection, cells were washed with serum-free DMEM and incubated with freshly delipidated 5% FBS DMEM supplemented with either compounds or DMSO vehicle for 24 h. After incubation, cell lysates were obtained using cell lysis buffer, and a luciferase activity assay was performed upon substrate addition using a MicroLumat Plus Luminometer (Berthold). The luciferase activity was normalized with β -galactosidase activity using an ONPG buffer. All assays were performed in triplicate.

Cytotoxicity assay

The *in vitro* cytotoxicity of **5a** was evaluated using the EZ-Cytox assay kit (DoGenBio, South Korea). BV-2 microglia or primary mouse astrocytes were seeded in 96-well clear microplates and treated with **5a** or GW501516 for 24 h at 37 °C. Absorbance was measured at 450 nm, after 1 h of incubation with EZ-Cytox containing water-soluble tetrazolium salt (WST), using a SpectraMaxⁱ³ microplate reader (Molecular Devices).

Griess assay for nitrite measurement

The nitric oxide (NO) released into the culture medium was quantified by measuring nitrite levels using the Griess method. BV-2 microglia were treated with **5a** or GW501516 for 3 h and stimulated with LPS (0.2 μ g/ml) for another additional 24 h. Primary mouse astrocytes were pretreated with compounds for 6 h and stimulated with LPS (100 ng/ml)/IFN γ (1 ng/ml) for 42 h. Culture media were collected and centrifugated at 2356 g for 3 min to remove large cell debris. The supernatants were incubated with equal amounts of sulfanilamide solution (1% sulfanilamide in 5% phosphoric acid) for 5 min in a 96-well

microplate, followed by NED solution (0.1% N-1-naphthylethylenediamine dihydrochloride in water) for 5 min at room temperature (20–25 °C) in the dark. Nitrite concentrations were determined by measuring the absorbance at 540 nm using a SpectraMaxⁱ³ microplate reader (Molecular Devices) based on a standard reference curve prepared with 0.1 M sodium nitrite.

Quantitative real-time reverse-transcription PCR (qRT-PCR) analysis

Total RNA was isolated using TRIzol[®] (Invitrogen). Genomic DNA was removed and complementary DNA was synthesized from 500 ng total RNA using the iScript[™] gDNA Clear cDNA Synthesis Kit (Bio-Rad). Real-time PCR was performed using the CFX Connect[™] Real-Time PCR Detection System (Bio-Rad) using iQ[™] SYBR[®] Green Supermix (Bio-Rad). The hypoxanthine phosphoribosyltransferase (*Hprt*) was used to normalize mRNA expression levels. Primer sequences used are described in Table S6.

Western blotting

Total proteins were extracted from cells or mouse brain tissues using radioimmunoprecipitation assay (RIPA) buffer (Sigma-Aldrich) containing a protease and phosphatase inhibitor cocktail (Roche Diagnostics). After 30 min of incubation with RIPA buffer on ice, lysates were centrifuged at 15800 g and 4 °C for 20 min and supernatants were collected. Protein concentrations were determined using Pierce[®] BCA Protein Assay Kit (Thermo Fisher Scientific). Protein samples (10 μ g) were separated on 10% SDS-PAGE gels and transferred to polyvinylidene fluoride (PVDF) membranes (Millipore). The membranes were blocked in 5% skim milk (Millipore) in TBST (10 mM Tris-HCl, pH 7.5, 150 mM NaCl, and 0.1% Tween[®] 20) for 1 h at room temperature and incubated overnight at 4 °C with primary antibodies. After washing three times with TBST, the membranes were incubated with horseradish peroxidase-conjugated anti-mouse or anti-rabbit IgG (GeneTex) for 1 h at room temperature and then developed with SuperLumina ECL HRP Substrate solution (Abbkine) using the Amersham Imager 600 (GE Healthcare). The western blot bands were analyzed using ImageJ software (NIH) and β -Actin or glyceraldehyde 3-phosphate dehydrogenase (GAPDH) were used as a loading control. Primary antibodies used are described in Table S6.

Enzyme-linked immunosorbent assay (ELISA)

The concentration of pro-inflammatory cytokines in the cell culture medium or mouse plasma was determined using ELISA kits for mouse TNF α

(Invitrogen, 88-7324-88) and IL-6 (Invitrogen, 88-7064-88). BV-2 microglia were treated with **5a** or GW501516 for 9 h followed by LPS (0.2 µg/ml) stimulation for 18 h. Primary mouse astrocytes were treated with compounds for 24 h followed by LPS (10 ng/ml)/IFN γ (1 ng/ml) stimulation for 12 h, and the culture medium was used for analysis. Mouse plasma samples were obtained by centrifuging blood collected from the heart at 848 g and 4 °C for 15 min. Absorbance was measured at 450 nm using a SpectraMax[®]i3 microplate reader (Molecular Devices).

Fluorescence imaging of intracellular ROS

Intracellular ROS accumulation was monitored using the cell-permeable fluorescent probe DCFH-DA (Sigma-Aldrich). BV-2 microglia were seeded in 96-well black plates and treated with **5a** or GW501516 for 24 h at 37 °C. The cells were loaded with 40 µM DCFH-DA in culture medium for 40 min at 37 °C in the dark. Then, 200 µM H₂O₂ was added to the medium for an additional 20 min at 37 °C. After washing with phosphate-buffered saline (PBS), cells were imaged with an ImageXpress Pico (Molecular Devices) and fluorescence intensity was quantified using the ImageJ software (NIH).

Animals and treatment

All mice and rats were housed in a temperature- and humidity-controlled environment with a 12 h light/dark cycle and ad libitum access to food and water. All procedures were performed in accordance with the National Institutes of Health Guide for the Care and Use of Laboratory Animals and approved by the Institutional Animal Care and Use Committee of Korea Institute of Science and Technology (KIST-IACUC-2022-020-1). For the pharmacokinetics study, Sprague-Dawley rats were purchased from Koatech (South Korea) and maintained in a specific pathogen-free facility (Laboratory Animal Center, Daegu-Gyeongbuk Medical Innovation Foundation). For the LPS-induced neuroinflammation model or scopolamine-induced AD model, male C57BL/6N mice were obtained from DBL (South Korea). APP/PS1 (APP_{swe}/PSEN1dE9) transgenic mice from the Jackson Laboratory (USA; stock number 004462) were maintained as hemizygotes on the C57BL/6; C3H genetic background at the Research Animal Resources Center of KIST. 10-week-old C57BL/6N and 12-month-old APP/PS1 were used in behavioral experiments with sex- and age-matched controls.

Compound **5a** and GW501516 (Combi-Blocks, QJ-9419) were dissolved in distilled water and orally administered once per day for the duration of the experiment. For the neuroinflammation model, C57BL/6N mice were intraperitoneally injected daily with 0.3 mg/kg LPS (Sigma-Aldrich, L2880) dissolved

in saline (0.9% sodium chloride), for 6 consecutive days. In a non-genetic AD model, we induced acute memory deficits in C57BL/6N mice by intraperitoneal injection with 1 mg/kg of scopolamine hydrobromide (Sigma-Aldrich, S0929) dissolved in saline, 30 min before the behavioral tests. At the end of the experimental period, mice were deeply anesthetized with 2% avertin (500 mg/kg, *i.p.*) and transcardially perfused with saline. Brains were collected from each mouse, and the hippocampus and cortex were isolated and stored at -80 °C for biochemical analysis. Brain hemispheres were postfixed in 4% paraformaldehyde overnight at 4 °C, then placed in 30% sucrose solution for 48 h at 4 °C for cryoprotection and used for histological analysis.

Open-field test

The locomotor activity in mice was assessed using the open-field test. Mice were placed in the center of a white square chamber (40 cm × 40 cm × 30 cm). All movements were recorded for 5 min and analyzed by an automated tracking software Ethovision XT 11.5 (Noldus). The center zone was defined as a 20 cm × 20 cm area in the center of the chamber.

Y-maze test

The Y-maze test was used to evaluate the spatial learning and memory performance of mice. The Y-maze apparatus consisted of three identical arms disposed at a 120° angle from each other (41 cm long and 7 cm wide with 15 cm high walls). Mice were placed at the end of one arm and allowed to move freely in the maze for 10 min. The arm entries were manually recorded. Spontaneous alternation was defined as consecutive entries into three different arms and the percentage of alternation was calculated based on the following equation: alternation (%) = number of alternations / (total arm entries - 2) × 100.

Passive avoidance test

The passive avoidance test was performed in two compartments, a light room and a dark room, separated by a guillotine door (GEMINI Avoidance System, San Diego Instruments). On the first experimental day, mice were placed in the light room for the acquisition trial. After exploration for 30 s, the guillotine door was raised and the mice were allowed to enter the dark room spontaneously. When the mice crossed the door, the door was closed and 3 s later an electric foot shock (0.4 mA, 1 s duration) was applied. The mice remained in the dark room for an additional 30 s and then were returned to their home cages. Twenty-four hours after the acquisition trial, the mice were placed again in the light room and the door was raised after 15 s. The step-through latency to enter the

dark room was automatically measured using GEMINI software (San Diego Instruments).

Morris water maze test

The spatial learning and memory performance of mice was assessed using the Morris water maze test. A white circular tank (150 cm in diameter, 58 cm in height) was filled with water at a temperature of 24 – 25 °C and a white circular platform (20 cm in diameter) was placed 1.5 cm lower than the water surface, and white non-toxic tempera paint was dissolved in water so that the mice could not visually determine the location of the platform. The water maze was divided into quadrants, and mice were released at each of the four points. To enable the mice to recognize each direction, spatial cues of different shapes were placed on the wall in the north, east, and south directions. In acquisition tests for 7 days, mice were trained to find the platform 4 times a day at each releasing point for 60 s. In a probe test on day 8, mice were allowed to swim freely for 100 s with the platform removed. All trials were recorded and automatically analyzed using the EthoVision XT 11.5 (Noldus). The target zone in the probe test was defined as an area with a radius of 30 cm centered on the platform during the acquisition test.

Immunofluorescence staining

Fixed mouse brains were embedded in an optimal cutting temperature compound (Leica, 3801480) and serially sectioned at 30 µm in a cryostat (Thermo Fisher Scientific, HM525 NX). Coronal hippocampal sections were stored in a storage solution (30% glycerol, 30% ethylene glycol, and 30% 0.2 M sodium phosphate buffer, pH 7.2) at 4 °C until use. After washing three times with PBS, the sections were blocked for 1 h with blocking buffer (0.3% Triton X-100 and 4% normal donkey serum in 0.1 M PBS) at room temperature, followed by incubation with primary antibodies in blocking buffer overnight at 4 °C. After washing with PBS, the sections were incubated with corresponding fluorescent secondary antibodies (Jackson ImmunoResearch, Alexa Fluor) for 1 h at room temperature and washed three times with PBS. Nuclei were counterstained with 4',6-diamidino-2-phenylindole (DAPI; Invitrogen) during the second washing step. Sections were mounted with fluorescent mounting medium (Dako). Fluorescent images were acquired with the ImageXpress Pico (Molecular Devices; 20× magnification) or LSM 800 confocal microscope (Carl Zeiss; 40× magnification). Primary antibodies used are described in Table S6.

Image quantification

Z-stack projected images (20 µm thickness with a

step size of 2 µm or 4 µm) were analyzed using the ImageJ software (NIH). To quantify glial reactivity, the mean fluorescence intensity of GFAP or IBA1 was measured. To evaluate microglial M1 polarization, the mean fluorescence intensity of CD86 was measured in the IBA1 staining-positive area. In CD86 and IBA1 double-stained sections, IBA1-immunostained pixels were defined as a region of interest after thresholding. For the analysis of plaque-associated BACE1, the fluorescence intensity of BACE1 or 6E10 was measured along a 200 µm² area around 6E10-positive amyloid plaque using the 'Plot Profile' function of ImageJ software (NIH). To quantify tau phosphorylation levels, the AT8-stained area was measured within a 50 µm range of the thioflavin S-positive plaque. To assess microglial Aβ phagocytosis, within a 50 µm range of the 6E10-positive plaque, the number of IBA1-positive microglia was counted and the CD68-positive area was measured in the IBA1 or 6E10-positive area.

Morphological analysis of astrocytes

Confocal z-stack images (20 µm thickness with 2 µm step size; under 40× magnification) were analyzed using the 'Sholl Analysis' function of ImageJ software (NIH). Individual GFAP-positive astrocytes in the hippocampal dentate gyrus were maximally projected and converted to binary images by thresholding. Continuous concentric circles were drawn at 3.125 µm intervals from the center of the soma. The maximum length of astrocytic processes (ending radius), total number of intersections per concentric circle (sum intersections), and ramification index were automatically calculated.

Thioflavin-S staining

Aβ plaques in APP/PS1 mouse brains were labeled with thioflavin-S (Sigma-Aldrich, T1892). Coronal brain sections were incubated for 8 min with 1 mM thioflavin-S dissolved in 50% ethanol and washed two times with 80% ethanol and three times with PBS. Stained sections were mounted on slides with fluorescent mounting medium (Dako) and visualized with the ImageXpress Pico (Molecular Devices). For plaque analysis, the number and area of plaques in the cortex or hippocampus were quantified using the 'Analyze Particles' function of ImageJ software (NIH).

Statistical analysis

Data were analyzed with GraphPad Prism 7 software and presented as mean ± SEM. The statistical significance of differences between the two groups was determined using an unpaired two-tailed Student's t-test. Multiple comparisons between groups were performed with one-way analysis of

variance (ANOVA) followed by Tukey's or Dunnett's *post-hoc* test and repeated measures one-way ANOVA followed by Fisher's LSD test. The statistical significance level is displayed as asterisks (* $P < 0.05$, ** $P < 0.01$, *** $P < 0.001$, and **** $P < 0.0001$; n.s. not significant).

Abbreviations

AD: Alzheimer's disease; ADMET: absorption, distribution, metabolism, excretion, and toxicity; ANGPTL4: Angiopoietin-like 4; A β : amyloid β ; BACE1: beta-secretase 1; CD: cluster of differentiation; CNS: central nervous system; CYP: cytochrome P450; DTT: dithiothreitol; EC₅₀: half maximal effective concentration; FBS: fetal bovine serum; GFAP: glial fibrillary acidic protein; hERG: human ether-à-go-go-related gene; HO-1: heme oxygenase-1; HPLC: high-performance liquid chromatography; IBA1: ionized calcium-binding adaptor molecule 1; IFN γ : interferon γ ; IL: interleukin; iNOS: inducible nitric oxide synthase; LBD: ligand-binding domain; LPS: lipopolysaccharide; MS: mass spectrometry; NF- κ B: nuclear factor- κ B; NO: nitric oxide; PDK4: pyruvate dehydrogenase kinase 4; PK: pharmacokinetic; PPAR: peroxisome proliferator-activated receptor; PPRE: peroxisome proliferator response element; ROS: reactive oxygen species; THF: tetrahydrofuran; TNF: tumor necrosis factor; WT: wild type.

Supplementary Material

Supplementary methods, results, spectra, figures.
<https://www.thno.org/v14p6088s1.pdf>

Acknowledgments

This study was supported by the Korea Institute of Science and Technology (KIST) Institutional Program (2E32161), the Basic Science Research Program funded by the Ministry of Science and ICT (2019R1A2C2005492, NRF-2021M3A9G1016475), the Korea Dementia Research Project through the Korea Dementia Research Center (KDRC) funded by the Ministry of Health & Welfare and Ministry of Science and ICT (HU23C0018), and Basic Science Research Program through the National Research Foundation of Korea (NRF) funded by the Ministry of Education (RS-2023-00273147).

Author contributions

H.J.K., J.Y.H., H.H., and J.-H.P. performed biological experiments. H.K., J.S., A.M.L., H.Y., J.H.B., and A.N.P. performed the X-ray crystallographic analysis and molecular docking studies. E.H.L., J.W.C., S.J.P., E.O., D.H., K.J., S.K., and T.M.K. synthesized the compounds. S.J.C., J.C., H.K., and

K.D.P. designed and supervised this study. All authors approved the final version of the manuscript.

Competing Interests

The authors have declared that no competing interest exists.

References

1. Issemann I, Green S. Activation of a member of the steroid hormone receptor superfamily by peroxisome proliferators. *Nature*. 1990; 347: 645-50.
2. Tyagi S, Gupta P, Saini AS, Kaushal C, Sharma S. The peroxisome proliferator-activated receptor: A family of nuclear receptors role in various diseases. *J Adv Pharm Technol Res*. 2011; 2: 236-40.
3. Corton JC, Anderson SP, Stauber A. Central Role of Peroxisome Proliferator-Activated Receptors in the Actions of Peroxisome Proliferators. *Annu Rev Pharmacol Toxicol*. 2000; 40: 491-518.
4. Berger J, Moller DE. The Mechanisms of Action of PPARs. *Annu Rev Med*. 2002; 53: 409-35.
5. Wang Y-X. PPARs: diverse regulators in energy metabolism and metabolic diseases. *Cell Res*. 2010; 20: 124-37.
6. Kadayat TM, Shrestha A, Jeon YH, An H, Kim J, Cho SJ, et al. Targeting Peroxisome Proliferator-Activated Receptor Delta (PPAR δ): A Medicinal Chemistry Perspective. *J Med Chem*. 2020; 63: 10109-34.
7. Hong F, Pan S, Guo Y, Xu P, Zhai Y. PPARs as Nuclear Receptors for Nutrient and Energy Metabolism. *Molecules*. 2019; 24: 2545.
8. Moreno S, Farioli-Vecchioli S, Cerù MP. Immunolocalization of peroxisome proliferator-activated receptors and retinoid x receptors in the adult rat CNS. *Neuroscience*. 2004; 123: 131-45.
9. Gofflot F, Chartoire N, Vasseur L, Heikkinen S, Dembele D, Le Merrer J, et al. Systematic Gene Expression Mapping Clusters Nuclear Receptors According to Their Function in the Brain. *Cell*. 2007; 131: 405-18.
10. Warden A, Truitt J, Merriman M, Ponomareva O, Jameson K, Ferguson LB, et al. Localization of PPAR isotypes in the adult mouse and human brain. *Sci Rep*. 2016; 6: 27618.
11. Woods JW, Tanen M, Figueroa DJ, Biswas C, Zychband E, Moller DE, et al. Localization of PPAR δ in murine central nervous system: expression in oligodendrocytes and neurons. *Brain Res*. 2003; 975: 10-21.
12. Cristiano L, Cimini A, Moreno S, Ragnelli AM, Paola Cerù M. Peroxisome Proliferator-Activated Receptors (PPARs) and related transcription factors in differentiating astrocyte cultures. *Neuroscience*. 2005; 131: 577-87.
13. Jana M, Pahan K. Gemfibrozil, a Lipid Lowering Drug, Inhibits the Activation of Primary Human Microglia Via Peroxisome Proliferator-Activated Receptor β . *Neurochem Res*. 2012; 37: 1718-29.
14. Varga T, Czimmerer Z, Nagy L. PPARs are a unique set of fatty acid regulated transcription factors controlling both lipid metabolism and inflammation. *Biochim Biophys Acta Mol Basis Dis*. 2011; 1812: 1007-22.
15. Daynes RA, Jones DC. Emerging roles of PPARs in inflammation and immunity. *Nat Rev Immunol*. 2002; 2: 748-59.
16. Hall MG, Quignodon L, Desvergne B. Peroxisome Proliferator-Activated Receptor β/δ in the Brain: Facts and Hypothesis. *PPAR Res*. 2008; 2008: 780452.
17. Schnegg CI, Robbins ME. Neuroprotective Mechanisms of PPAR δ : Modulation of Oxidative Stress and Inflammatory Processes. *PPAR Res*. 2011; 2011: 373560.
18. Strosznajder AK, Wójtowicz S, Jeżyna MJ, Sun GY, Strosznajder JB. Recent Insights on the Role of PPAR- β/δ in Neuroinflammation and Neurodegeneration, and Its Potential Target for Therapy. *Neuromolecular Med*. 2021; 23: 86-98.
19. Dickey AS, Pineda VV, Tsunemi T, Liu PP, Miranda HC, Gilmore-Hall SK, et al. PPAR- δ is repressed in Huntington's disease, is required for normal neuronal function and can be targeted therapeutically. *Nat Med*. 2016; 22: 37-45.
20. Dickey AS, Sanchez DN, Arreola M, Sampat KR, Fan W, Arbez N, et al. PPAR δ activation by bexarotene promotes neuroprotection by restoring bioenergetic and quality control homeostasis. *Sci Transl Med*. 2017; 9: eal2332.
21. Kuang G, He Q, Zhang Y, Zhuang R, Xiang A, Jiang Q, et al. Modulation of Preactivation of PPAR- β on Memory and Learning Dysfunction and Inflammatory Response in the Hippocampus in Rats Exposed to Global Cerebral Ischemia/Reperfusion. *PPAR Res*. 2012; 2012: 209794.
22. Chen L, Xue L, Zheng J, Tian X, Zhang Y, Tong Q. PPAR β/δ agonist alleviates NLRP3 inflammasome-mediated neuroinflammation in the

- MPTP mouse model of Parkinson's disease. *Behav Brain Res.* 2019; 356: 483-9.
23. Polak PE, Kalinin S, Dello Russo C, Gavriluyk V, Sharp A, Peters JM, et al. Protective effects of a peroxisome proliferator-activated receptor- β/δ agonist in experimental autoimmune encephalomyelitis. *J Neuroimmunol.* 2005; 168: 65-75.
 24. Chehaibi K, le Maire L, Bradoni S, Escola JC, Blanco-Vaca F, Slimane MN. Effect of PPAR- β/δ agonist GW0742 treatment in the acute phase response and blood-brain barrier permeability following brain injury. *Transl Res.* 2017; 182: 27-48.
 25. Peters JM, Lee SST, Li W, Ward JM, Gavrilova O, Everett C, et al. Growth, Adipose, Brain, and Skin Alterations Resulting from Targeted Disruption of the Mouse Peroxisome Proliferator-Activated Receptor $\beta(\delta)$. *Mol Cell Biol.* 2000; 20: 5119-28.
 26. Nadra K, Anghel SI, Joye E, Tan NS, Basu-Modak S, Trono D, et al. Differentiation of Trophoblast Giant Cells and Their Metabolic Functions Are Dependent on Peroxisome Proliferator-Activated Receptor β/δ . *Mol Cell Biol.* 2006; 26: 3266-81.
 27. Masters CL, Bateman R, Blennow K, Rowe CC, Sperling RA, Cummings JL. Alzheimer's disease. *Nat Rev Dis Primers.* 2015; 1: 15056.
 28. Heppner FL, Ransohoff RM, Becher B. Immune attack: the role of inflammation in Alzheimer disease. *Nat Rev Neurosci.* 2015; 16: 358-72.
 29. Kinney JW, Bemiller SM, Murtishaw AS, Leisgang AM, Salazar AM, Lamb BT. Inflammation as a central mechanism in Alzheimer's disease. *Alzheimers Dement Transl Res Clin Interv.* 2018; 4: 575-90.
 30. de la Monte SM, Wands JR. Molecular indices of oxidative stress and mitochondrial dysfunction occur early and often progress with severity of Alzheimer's disease. *J Alzheimers Dis.* 2006; 9: 167-81.
 31. An Y-Q, Zhang CT, Du Y, Zhang M, Tang SS, Hu M, et al. PPAR δ agonist GW0742 ameliorates A β 1-42-induced hippocampal neurotoxicity in mice. *Metab Brain Dis.* 2016; 31: 663-71.
 32. Barroso E, del Valle J, Porquet D, Vieira Santos AM, Salvadó L, Rodríguez-Rodríguez R, et al. Tau hyperphosphorylation and increased BACE1 and RAGE levels in the cortex of PPAR β/δ -null mice. *Biochim Biophys Acta Mol Basis Dis.* 2013; 1832: 1241-8.
 33. Kalinin S, Richardson JC, Feinstein DL. A PPAR δ Agonist Reduces Amyloid Burden and Brain Inflammation in a Transgenic Mouse Model of Alzheimers Disease. *Curr Alzheimer Res.* 2009; 6: 431-7.
 34. Malm T, Mariani M, Donovan LJ, Neilson L, Landreth GE. Activation of the nuclear receptor PPAR δ is neuroprotective in a transgenic mouse model of Alzheimer's disease through inhibition of inflammation. *J Neuroinflammation.* 2015; 12: 7.
 35. Tong M, Deochand C, Didsbury J, de la Monte SM. T3D-959: A Multi-Faceted Disease Remedial Drug Candidate for the Treatment of Alzheimer's Disease. *J Alzheimers Dis.* 2016; 51: 123-38.
 36. de la Monte SM, Tong M, Schiano J, Didsbury J. Improved Brain Insulin/IGF Signaling and Reduced Neuroinflammation with T3D-959 in an Experimental Model of Sporadic Alzheimer's Disease. *J Alzheimers Dis.* 2017; 55: 849-64.
 37. Reich D, Gallucci G, Tong M, de la Monte SM. Therapeutic Advantages of Dual Targeting of PPAR- δ and PPAR- γ in an Experimental Model of Sporadic Alzheimer's Disease. *J Parkinsons Dis Alzheimers Dis.* 2018; 5: 8.
 38. Chamberlain S, Gabriel H, Strittmatter W, Didsbury J. An Exploratory Phase IIa Study of the PPAR delta/gamma Agonist T3D-959 Assessing Metabolic and Cognitive Function in Subjects with Mild to Moderate Alzheimer's Disease. *J Alzheimers Dis.* 2020; 73: 1085-103.
 39. Wu C-C, Baiga TJ, Downes M, La Clair JJ, Atkins AR, Richard SB, et al. Structural basis for specific ligation of the peroxisome proliferator-activated receptor δ . *Proc Natl Acad Sci U S A.* 2017; 114: E2563-70.
 40. Cox RL. Rationally designed PPAR δ -specific agonists and their therapeutic potential for metabolic syndrome. *Proc Natl Acad Sci U S A.* 2017; 114: 3284-5.
 41. Da'adoosh B, Marcus D, Rayan A, King F, Che J, Goldblum A. Discovering highly selective and diverse PPAR-delta agonists by ligand based machine learning and structural modeling. *Sci Rep.* 2019; 9: 1106.
 42. Kaminski R, Glass RS, Skowronska A. A convenient synthesis of selenocarboxamides from nitriles. *Synthesis.* 2001; 2001: 1308-10.
 43. Batista FAH, Trivella DBB, Bernardes A, Gratieri J, Oliveira PSL, Figueira ACM, et al. Structural Insights into Human Peroxisome Proliferator Activated Receptor Delta (PPAR-Delta) Selective Ligand Binding. *PLoS One.* 2012; 7: e33643.
 44. Korbecki J, Bobiński R, Dutka M. Self-regulation of the inflammatory response by peroxisome proliferator-activated receptors. *Inflamm Res.* 2019; 68: 443-58.
 45. Sodhi K, Puri N, Kim DH, Hinds TD, Stechschulte LA, Favero G, et al. PPAR δ binding to heme oxygenase 1 promoter prevents angiotensin II-induced adipocyte dysfunction in Goldblatt hypertensive rats. *Int J Obes.* 2014; 38: 456-65.
 46. Campbell NK, Fitzgerald HK, Dunne A. Regulation of inflammation by the antioxidant haem oxygenase 1. *Nat Rev Immunol.* 2021; 21: 411-25.
 47. Yeh P-Y, Li C-Y, Hsieh C-W, Yang Y-C, Yang P-M, Wung B-S. CO-releasing molecules and increased heme oxygenase-1 induce protein S-glutathionylation to modulate NF- κ B activity in endothelial cells. *Free Radic Biol Med.* 2014; 70: 1-13.
 48. Dantzer R, O'Connor JC, Freund GG, Johnson RW, Kelley KW. From inflammation to sickness and depression: when the immune system subjugates the brain. *Nat Rev Neurosci.* 2008; 9: 46-56.
 49. Lasselin J, Schedlowski M, Karshikoff B, Engler H, Lekander M, Komsan JP. Comparison of bacterial lipopolysaccharide-induced sickness behavior in rodents and humans: Relevance for symptoms of anxiety and depression. *Neurosci Biobehav Rev.* 2020; 115: 15-24.
 50. Batista CR, Gomes GF, Candelario-Jalil E, Fiebich BL, de Oliveira AC. Lipopolysaccharide-Induced Neuroinflammation as a Bridge to Understand Neurodegeneration. *Int J Mol Sci.* 2019; 20: 2293.
 51. Perry VH, Cunningham C, Holmes C. Systemic infections and inflammation affect chronic neurodegeneration. *Nat Rev Immunol.* 2007; 7: 161-7.
 52. Acosta C, Anderson HD, Anderson CM. Astrocyte dysfunction in Alzheimer disease. *J Neurosci Res.* 2017; 95: 2430-47.
 53. Liddelow SA, Guttenplan KA, Clarke LE, Bennett FC, Bohlen CJ, Schirmer L, et al. Neurotoxic reactive astrocytes are induced by activated microglia. *Nature.* 2017; 541: 481-7.
 54. Lee WJ, Ham SA, Lee GH, Choi M-J, Yoo H, Paek KS, et al. Activation of peroxisome proliferator-activated receptor delta suppresses BACE1 expression by up-regulating SOCS1 in a JAK2/STAT1-dependent manner. *J Neurochem.* 2019; 151: 370-85.
 55. Zhao J, Fu Y, Yasvoina M, Shao P, Hitt B, Connor T, et al. β -Site Amyloid Precursor Protein Cleaving Enzyme 1 Levels Become Elevated in Neurons around Amyloid Plaques: Implications for Alzheimer's Disease Pathogenesis. *J Neurosci.* 2007; 27: 3639.
 56. Zhang X-M, Cai Y, Xiong K, Cai H, Luo X-G, Feng J-C, et al. β -Secretase-1 elevation in transgenic mouse models of Alzheimer's disease is associated with synaptic/axonal pathology and amyloidogenesis: implications for neuritic plaque development. *Eur J Neurosci.* 2009; 30: 2271-83.
 57. Kandalepas PC, Sadleir KR, Eimer WA, Zhao J, Nicholson DA, Vassar R. The Alzheimer's β -secretase BACE1 localizes to normal presynaptic terminals and to dystrophic presynaptic terminals surrounding amyloid plaques. *Acta Neuropathol.* 2013; 126: 329-52.
 58. Sturchler-Pierrat C, Abramowski D, Duke M, Wiederhold K-H, Mistl C, Rothacher S, et al. Two amyloid precursor protein transgenic mouse models with Alzheimer disease-like pathology. *Proc Natl Acad Sci U S A.* 1997; 94: 13287-92.
 59. Li T, Braunstein KE, Zhang J, Lau A, Sibener L, Deeble C, et al. The neuritic plaque facilitates pathological conversion of tau in an Alzheimer's disease mouse model. *Nat Commun.* 2016; 7: 12082.
 60. Karran E, De Strooper B. The amyloid hypothesis in Alzheimer disease: new insights from new therapeutics. *Nat Rev Drug Discov.* 2022; 21: 306-18.
 61. Rodríguez-Calvo R, Serrano La, Coll T, Moullan N, Sánchez RM, Merlos M, et al. Activation of Peroxisome Proliferator-Activated Receptor β/δ Inhibits Lipopolysaccharide-Induced Cytokine Production in Adipocytes by Lowering Nuclear Factor- κ B Activity via Extracellular Signal-Related Kinase 1/2. *Diabetes.* 2008; 57: 2149-57.
 62. Kapoor A, Shintani Y, Collino M, Osuchowski MF, Busch D, Patel NS, et al. Protective role of peroxisome proliferator-activated receptor- β/δ in septic shock. *Am J Respir Crit Care Med.* 2010; 182: 1506-15.
 63. Lee WJ, Ham SA, Yoo H, Hwang JS, Yoo T, Paek KS, et al. Activation of PPAR δ attenuates neurotoxicity by inhibiting lipopolysaccharide-triggered glutamate release in BV-2 microglial cells. *J Cell Biochem.* 2018; 119: 5609-19.
 64. Defaux A, Zurich M-G, Braissant O, Honegger P, Monnet-Tschudi F. Effects of the PPAR- β agonist GW01516 in an in vitro model of brain inflammation and antibody-induced demyelination. *J Neuroinflammation.* 2009; 6: 15.
 65. Haskova Z, Hoang B, Luo G, Morgan LA, Billin AN, Barone FC, et al. Modulation of LPS-induced pulmonary neutrophil infiltration and cytokine production by the selective PPAR β/δ ligand GW0742. *Inflammation Res.* 2008; 57: 314-21.
 66. Lee HJ, Yeon JE, Ko EJ, Yoon EL, Suh SJ, Kang K, et al. Peroxisome proliferator-activated receptor-delta agonist ameliorated inflammasome activation in nonalcoholic fatty liver disease. *World J Gastroenterol.* 2015; 21: 12787-99.
 67. Sastre M, Dewachter I, Rossner S, Bogdanovic N, Rosen E, Borghgraef P, et al. Nonsteroidal anti-inflammatory drugs repress β -secretase gene

- promoter activity by the activation of PPAR γ . *Proc Natl Acad Sci U S A*. 2006; 103: 443-8.
68. Salter MW, Stevens B. Microglia emerge as central players in brain disease. *Nat Med*. 2017; 23: 1018-27.
 69. Leng F, Edison P. Neuroinflammation and microglial activation in Alzheimer disease: where do we go from here? *Nat Rev Neurol*. 2021; 17: 157-72.
 70. Mukundan L, Odegaard JI, Morel CR, Heredia JE, Mwangi JW, Ricardo-Gonzalez RR, et al. PPAR- δ senses and orchestrates clearance of apoptotic cells to promote tolerance. *Nat Med*. 2009; 15: 1266-72.
 71. Pettersen EF, Goddard TD, Huang CC, Couch GS, Greenblatt DM, Meng EC, et al. UCSF Chimera—A visualization system for exploratory research and analysis. *J Comput Chem*. 2004; 25: 1605-12.
 72. Otten JN, Hingorani GP, Hartley DP, Kragerud SD, Franklin RB. An in vitro, high throughput, seven CYP cocktail inhibition assay for the evaluation of new chemical entities using LC-MS/MS. *Drug Metab Lett*. 2011; 5: 17-24
 73. Lu C, Li P, Gallegos R, Uttamsingh V, Xia CQ, Miwa GT, et al. Comparison of Intrinsic Clearance in Liver Microsomes and Hepatocytes from Rats and Humans: Evaluation of Free Fraction and Uptake in Hepatocytes. *Drug Metab Dispos*. 2006; 34: 1600-5.
 74. Piper DR, Duff SR, Eliason HC, Frazee WJ, Frey EA, Fuerstenau-Sharp M, et al. Development of the Predictor hERG Fluorescence Polarization Assay Using a Membrane Protein Enrichment Approach. *Assay Drug Dev Technol*. 2008; 6: 213-23.